Chapter 12
Flares: Nonthermal Particles

12.1 Flare Gamma-Rays

Information on the highest energies of particles produced during solar flares, measured in gamma-ray wavelengths with photon energies of $E \gtrsim 300$ keV, has been obtained by very few instruments on a routine basis in the new millennium, such as from the *Ramaty High-Energy Spectroscopic Imager (RHESSI)* and from the *Fermi* spacecraft, and occasionally from the CORONAS-F mission and the *INTErnational Gamma-Ray Astrophysics Laboratory (INTEGRAL)* ESA mission. Recent reviews can be found on energetic ions in solar flares from gamma-ray and neutron observations (Vilmer et al. (2011)), on electron acceleration and propagation in solar flares (Holman et al. 2011), and on future hard X-ray and gamma-ray spectroscopy (Holman 2016).

A key result of the RHESSI mission is the discovery of gamma-ray footpoint structures, obtained from the first gamma-ray images of a solar flare at all, observed during the X4.8-class flare on 2002 July 23. This event turned out to be also the largest solar flare observed by RHESSI. Double ion footpoints have been imaged at 2.223 MeV (where the spectrum is dominated by a gamma-ray line). The narrow deuterium line at 2.223 MeV is formed by the thermalization and capture of neutrons produced in collisions. The ion footpoints were found to be slightly but significantly displaced ($20'' \pm 6''$) from the electron precipitation sites usually seen in $\gtrsim 25$ keV hard X-rays (Fig. 12.1), which poses an interesting new problem for particle acceleration models in terms of the standard thick-target flare model (Hurford et al. 2003, 2006; Smith et al. 2003; Lin et al. 2003; Schrijver et al. 2006). The spectral line profiles of Ne, Mg, Si, Fe, C, and O were for the first time resolved, exhibiting Doppler redshifts of 0.1%–0.8% and FWHM broadening of 0.1%–2.1%. Interpretations of the large redshifts in terms of inclined magnetic fields or extreme beaming of the ions were considered, while a bulk downward motion of the plasma
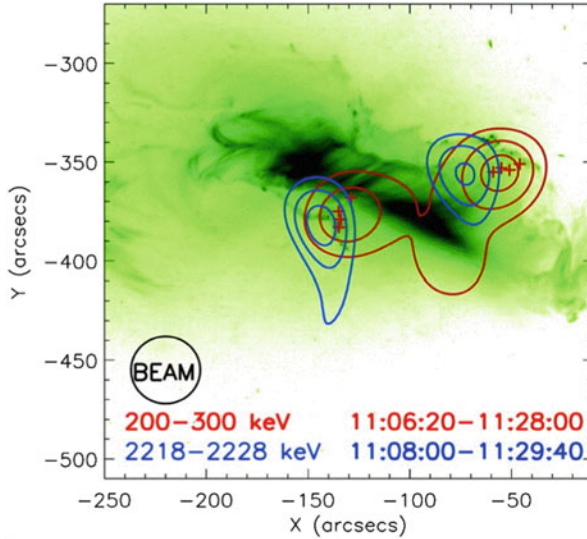
Fig. 12.1 Locations of the gamma-ray footpoint sources of the 2.2 MeV neutron capture line (blue contours) and the electron bremsstrahlung footpoint sources in the energy range of 200–300 keV, observed with RHESSI during the X4.8-class flare on 2002 July 23 (red contours). The green background image outlines the flare arcade as seen in EUV (from TRACE). The spatial resolution of RHESSI is indicated with a circular "beam size" pattern (Hurford et al. 2003)

in which the accelerated ions interact was ruled out (Smith et al. 2003). Other RHESSI-observed events with imaging of the neutron capture line include the flares of 2003 October 28, 2003 October 29, 2003 November 2 (Hurford et al. 2006), and 2005 January 20 (Masson et al. 2009; Kurt et al. 2010). The fact that the gamma-ray producing ions appear to be accelerated in highly localized regions (with a size of $\lesssim 20''$), indicates that they are accelerated by the coronal flare reconnection process, rather than by a widespread shock driven by a *coronal mass ejection (CME)* (Hurford et al. 2006; Lin 2006). Close correlations suggest that electrons with ≥ 0.3 MeV and protons with > 30 MeV are accelerated by a common mechanism (Shih et al. 2009).

Positron production by fast ions in solar flares may occur via the decay of radioactive daughter nuclei, beta decay of excited states of target nuclei, or via pion (plus) production, e.g., in $p(p, n\pi^+X)p'$. RHESSI resolved the spectral width of the 511 keV positron annihilation line, with a line width of typically $\gtrsim 5$ keV, which indicates a temperature of the accelerated-ion interaction region around $T \approx 10^5$ K, which is much higher than the expected value of $T \approx 10^4$ K in the chromosphere (Share et al. 2004). Although the energy contained in high-energy particles may have been enough to heat the plasma, the rate of deposition is not correlated with the temperature determined by the 511 keV line width, and this raises questions about the energy source (Share et al. 2004). Interactions of flare-accelerated ions in the solar atmosphere can synthesize radioactive nuclei, whose

decay can produce observable, delayed gamma-ray lines in the aftermath of large flares, which amounts to ≈ 2 days for the β^+ radioisotopes in the 511 keV positron-electron line (Tatischeff et al. 2006).

Only about 20 solar flare events have ever been observed with significant pion production, and 18 flares were detected with Fermi/LAT above > 100 MeV (Ackermann et al. 2014), and three of them behind the limb (Ackermann et al. 2017; Pesce-Rollins et al. 2015). Some of the most recent events have been observed in a wide energy range by both RHESSI and CORONAS-F (Kuznetsov et al. 2011; Trottet et al. 2008; Masson et al. 2009). Often there are two acceleration episodes, a first during the impulsive flare phase, and a second during a prolonged decay phase, lasting up to 20 hrs (Ajello et al. 2014). In the 2005 January 20 event, the first relativistic protons detected at Earth are accelerated together with relativistic electrons and with protons that produce pion-decay gamma-rays during the second episode (Masson et al. 2009). High-energy gamma radiation was detected with the *SOlar Neutrons and Gamma rays (SONG)* instrument onboard CORONAS-F up to energies of > 100 MeV, suggesting decay of neutral pions by > 300 MeV protons, as observed during the 2001 August 25, X5.3 flare (Kurt et al. 2010), and during the 2003 October 28, X17.2 flare (Kuznetsov et al. 2011).

Modeling of gamma-ray emission profiles, resulting from the bombardment of energetic ions impacting the chromosphere, using the observed nuclear de-excitation line profiles, requires an atmospheric model of the magnetic field, density, and temperature. A recent model addresses particle transport and interaction (in both hydrostatic and dynamically extended atmospheres) and includes energy losses due to Coulomb collisions, removal by nuclear reactions, magnetic mirroring in the converging magnetic flux, and MHD pitch-angle scattering in the corona, treated via the quasi-linear formalism (Murphy et al. 2007).

Quasi-periodic pulsations in gamma-ray emission have rarely been reported, probably because of insufficient signal-to-noise ratios, but a period of $P_1 \approx 40$ s has been detected during the solar flare of 2005 January 1, at photon energies up to 2–6 MeV with the SONG/CORONAS-F, as well as with RHESSI and the Nobeyama radio heliograph (Nakariakov et al. 2010). A second periodicity of $P_2 = 13$ s was noted also in the same flare, which was interpreted as second harmonic of the sausage MHD mode (Nakariakov et al. 2010).

12.2 Flare Hard X-Ray Ribbons

A common morphological structure of flares in the chromospheric regions is a pair of near-parallel *ribbons*, straddling along both sides of a magnetic polarity inversion line, and thus has conjugate (or opposite) magnetic polarity. The corresponding coronal structure is called a *flare arcade*, a sequence of nested loops that outline the post-reconnection magnetic field, with the footpoints anchored in the ribbons. The chromospheric double ribbons that are often visible in EUV, UV, or white-light, are generally not seen as a contiguous structure in hard X-rays, probably due to the

limited dynamic range of Fourier imaging, but RHESSI imaged larger segments of them in some flares (Fletcher and Hudson 2002; Liu et al. 2007; Dennis and Pernak 2009; Krucker et al. 2011). For a review see Fletcher et al. (2011).

Hard X-ray observations with the *Hard X-Ray Telescope (HXT)* onboard *Yohkoh* showed evidence for flare footpoint brightenings that precede the onset of the hard X-ray emission, but the spatio-temporal correlation indicates that the energy release occurs in different loops during the preflare and during the impulsive flare phase (Warren and Warshall 2001). The 2000 July 14 flare revealed for the first time > 30 keV hard X-ray emission along the entire two-ribbon structure, suggesting that magnetic reconnection and particle acceleration occurs in the entire flaring region (Masuda et al. 2001). Moreover, the transverse separation of the ribbons indicates that magnetic reconnection progresses from low-lying highly sheared loops in the beginning of the flare to higher-lying and less sheared loops near the top of the flare arcade (Masuda et al. 2001; Aschwanden and Alexander 2001; Fletcher and Hudson 2001). Also a correlation between the footpoint motion and the hard X-ray flux was found for this flare (Fletcher and Hudson 2002). The limb X1.5 flare of 2002 April 21 indeed showed a centroid motion of the thermal 12–25 keV source in upward direction, with an initial velocity of $v \approx 10$ km s^{-1}, confirming the interpretation that magnetic reconnection moves to higher altitudes, as predicted in classical flare models (Gallagher et al. 2002).

RHESSI observations provide higher spatial resolution than HXT/Yohkoh to trace the hard X-ray sources along flare ribbons, which is especially important for measuring the motion of the centroids of the relatively crude hard X-ray blobs (compared with the much thinner ribbons seen in EUV and Hα). During the 2002 July 23 gamma-ray flare, a systematic motion of the > 30 keV hard X-ray source along a ribbon was measured during a time interval of more than 10 min (Krucker et al. 2003), and similarly during the 2001 April 10 X2.3 flare (Asai et al. 2003). One of the longest hard X-ray ribbons was spotted in the 2005 May 13 flare (Fig. 12.2; Liu et al. 2007). Comparing Hα with UV/EUV flare ribbons, the flare ribbons have the tendency to spread systematically outwards of the magnetic polarity inversion line, while their appearance becomes more ordered as the flare progresses. On the other hand, the hard X-ray footpoint sources frequently move along the Hα or UV/EUV ribbons, while the ribbons move away from the polarity inversion line, and are found at locations distinguished by their high magnetic field strengths (Temmer et al. 2007), or their high magnetic flux transfer rates (Liu et al. 2008). The evolution of reconnection along two (conjugate) flare ribbons has been traced in detail in the 2002 November 9 flare and it was found that the reconnection process is not modulated simultaneously in the entire flare region, but occurs in a sequence of intermittent bursts that progresses along the flare arcade (Fig. 12.3; Grigis and Benz 2005).

The flare ribbon expansion can be used to test magnetic reconnection models (e.g. Qiu and Cheng 2017). The energy release rate can be written as a product of the Poynting flux into the reconnection region, $S = B_c^2 v_i / (4\pi)$, and the area of the
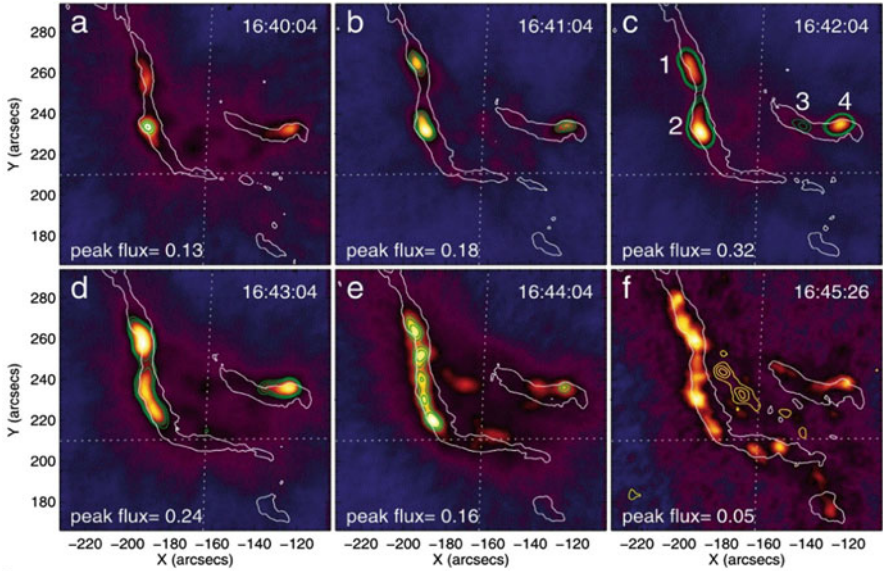
Fig. 12.2 The colored images represent a time sequence of RHESSI 25–50 keV hard X-ray images, integrated in 1 min time intervals. RHESSI images are reconstructed with the CLEAN algorithm. The white contours outline the TRACE 1600 Å ribbons taken near the center of each RHESSI time interval. Note the very long ribbon seen in hard X-rays (at the end of the flare, panel **f**), which almost matches the ribbon seen in ultraviolet at 1600 Å (Liu et al. 2007)
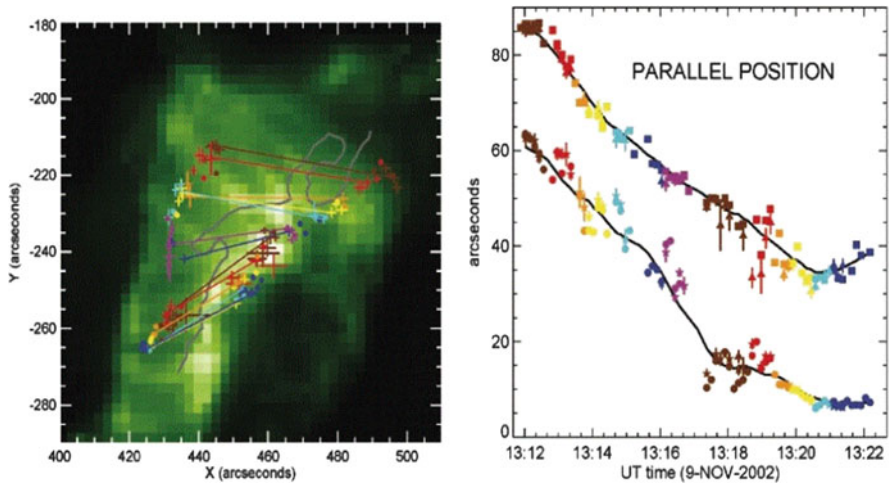
Fig. 12.3 *Left:* EIT/SOHO 195 Å image of the flare arcade observed during the 2002 November 12 flare. The colored lines indicate the magnetic connectivity at different times of the flare. *Right:* Time evolution of the source positions of the centroids of hard X-ray emission parallel to the ribbon curves. The color code marks different time intervals (Grigis and Benz 2005)

reconnection region, A, (Asai et al. 2004),

$$\frac{dE}{dt} = SA = 2\frac{B_c^2}{4\pi}v_i A \,, \tag{12.2.1}$$

where B_c is the magnetic field strength in the corona, and v_i is the inflow velocity into the reconnection region. With this method, Asai et al. (2004) found that the magnetic field strength of the Hα kernels associated with hard X-ray sources are about 3 times larger than those at the Hα kernels without hard X-ray sources. However, many flares display a more complex magnetic topology than envisioned from standard 2-D reconnection models, sometimes 3-D reconnection models are required that evolve as sigmoid-to-arcade transformations (Jing et al. 2007; Liu et al. 2007). The reconnection rates are never uniform along the flare ribbons, but are much larger at the locations where hard X-ray footpoints are observed (Temmer et al. 2007).

While most flare ribbons show some curvature, a few exhibit a completely circular geometry, which suggests a fan-spine magnetic topology involving reconnection at a 3-D coronal null point (Wang and Liu 2012). In the 2012 October 23 flare, three ribbons are visible, with two highly elongated ones inside and outside of a quasi-circular one, respectively (Yang et al. 2015). Many flares occur in a sigmoid geometry, where two J-shaped ribbons are matched, which are modeled with the inserted flux rope model and contain locations with prominent quasi-separatrix layers (Savcheva et al. 2015, 2016).

Modeling the energetics of flare ribbons with a temperature and emission measure analysis using GOES, EVE/SDO, AIA/SDO, and RHESSI data, substantial amounts of hot flare plasma (up to temperatures of $T_e \approx 10$ MK) was detected in the flare ribbons, during the pre-impulsive and early-impulsive flare phase (Fletcher et al. 2013).

The flare hard X-ray sources, which illuminate only short segments of the chromospheric flare ribbons at any time, generally appear as unresolved point sources (Dennis and Pernak 2009; Krucker et al. 2011), and may additionally be broadened by the theoretically predicted photospheric X-ray albedo. According to Kontar et al. (2006), back-reflected hard X-ray photons from the photosphere have been detected, where the solar surface acts like a *Compton mirror*.

12.3   Coronal Hard X-Rays

RHESSI provides imaging of hard X-rays within a dynamic range of about an order of magnitude, limited mostly by the fringes and sidelobes produced by Fourier imaging methods. During solar flares, the brightness of hard X-ray emission is generally strongest at the flaring footpoints (which are part of the flare ribbons), so that the fainter emission from coronal hard X-ray sources is outshone. If the bright footpoints are occulted by the solar limb, it is possible to detect much fainter

hard X-ray emission from coronal sources. Thus non-thermal hard X-ray emission is generally detected at the footpoints of flare loops (Krucker and Lin 2008), but RHESSI detects it also at coronal heights above flare loops (Battaglia and Benz 2007; Krucker et al. 2008; Ishikawa et al. 2011; Krucker et al. 2010), in occulted flares (Krucker et al. 2007b, 2010; Krucker and Lin 2008), in the preflare phase (Lin et al. 2003), in the absence of footpoint emission (Veronig and Brown 2004), associated with jets (Bain and Fletcher 2009), and cospatial with coronal mass ejections (Krucker et al. 2007a).

One of the most occulted flares occurred during 2002 October 27, which is associated with a SEP event and a very fast CME. Observed from Earth, the flare site is $40.4° \pm 3.5°$ behind the solar limb and the occultation height is $h = 1.5 \times 10^5$ km ≈ 0.35 $R_\odot$ (Krucker et al. 2007b). Acceleration of electrons appears to take place in the high corona, where about 10% of all electrons are nonthermal at ≥ 10 keV (Krucker et al. 2007a).

While the location of the primary magnetic reconnection process and the associated particle acceleration site has been identified earlier (with HXT/Yohkoh) at a coronal height h that corresponds roughly to a factor of $h/d \approx 1.5$ times the footpoint separation d, either from direct imaging of a limb flare (Masuda et al. 1994), or from electron time-of-flight measurements (Aschwanden et al. 1996). The new RHESSI observations went a step further and established double coronal X-ray Sources. RHESSI detected such double hard X-ray sources in some suitably oriented limb flares, which reveal a vertically symmetric energy gradient below and above a supposed X-point reconnection site (Figs. 12.4 and 12.5; Sui and Holman 2003; Liu et al. 2008). The higher energies in the inner region (relative to the X-point) show mainly nonthermal emission, while the outer regions show thermal emission (Liu et al. 2008). Below the X-point, *reconnection outflows* are predicted by the standard reconnection scenario, which indeed have been observed with TRACE during the 2002 July 23 flare (Asai et al. 2004).

Another novel discovery of RHESSI is the initial downward motion of the centroid of the nonthermal hard X-ray sources. This unexpected initial downward motion of coronal hard X-ray sources has been observed in a number of flares, apparently associated with the propagation of reconnection along flare ribbons (Sui et al. 2004; Veronig et al. 2006; Ji et al. 2008). Models with a collapsing trap embedded in a standard 2-D magnetic reconnection model fit the data, if the the loop top source is assumed to be thermal bremsstrahlung from "superhot" ($T \approx 35$–45 MK) plasma (Veronig et al. 2006).

The standard scenario of magnetic reconnection above a neutral inversion line predicts a progressive separation of the flare ribbons and related altitude increase of the magnetic reconnection X-point. A further consequence is that the footpoint reconnection rate (or reconnection speed) is proportional to the (non-thermal) hard X-ray flux (Eq. 12.2.1). In the X1.5-class flare of 2002 July 23 this is indeed the case in one footpoint ribbon, while it is not the case in the other (conjugate) footpoint ribbon (Lin et al. 2003).

Veronig and Brown (2004) identified a new class of solar hard X-ray-emitting flares that display no footpoints, which were interpreted as coronal flare loops
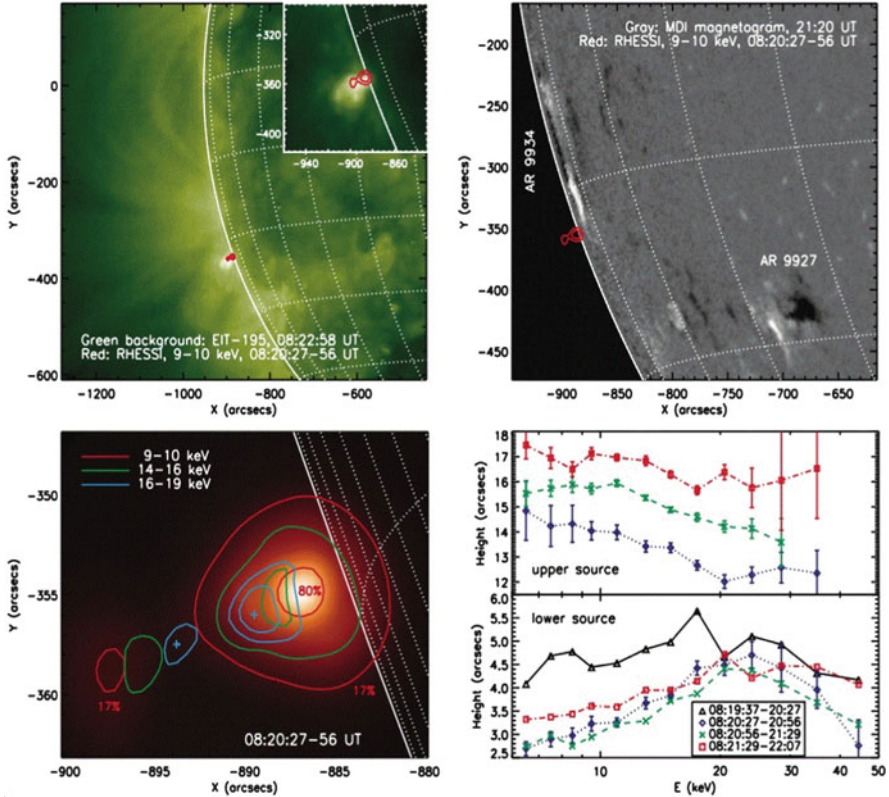
Fig. 12.4 Double coronal hard and soft X-ray sources observed by RHESSI, showing evidence for magnetic reconnection and particle acceleration. *Upper left:* EIT/SOHO 195 Å image observed at 2002 April 30, at 08:22 UT, superimposed with (red) RHESSI contours ot 9–10 keV. *Upper right:* MDI/SOHO magnetogram taken at 21:20 UT (some 13 hrs after the flare), overplotted with (red) RHESSI 9–10 keV contours. *Lower left:* RHESSI contours in three energy bands (9–10, 14–16, and 16–19 keV). *Lower right:* Height above the limb of the centroids for the upper and lower coronal sources, plotted as a function or energy, (Liu et al. 2008)

with such high densities that they are collisionally thick at electron energies up to $\gtrsim 50$ keV. It was shown that (i) the loop column densities are consistent with the nonthermal coronal thick-target model, (ii) chromospheric evaporation occurs by thermal conduction from the loop rather than by electron beam heating, and (iii) the hot loop temperature being in balance of thick-target collisional heating and (mainly) conductive heating (Veronig and Brown 2004).

Spectral analysis of coronal hard X-ray sources show soft-hard-soft evolution for both coronal and footpoint sources. However, the coronal source is nearly always softer than the footpoints (Battaglia and Benz 2006), which indicates that the location where electrons are accelerated to the highest energies (where they produce the hardest spectrum) lies between the coronal hard X-ray source and the
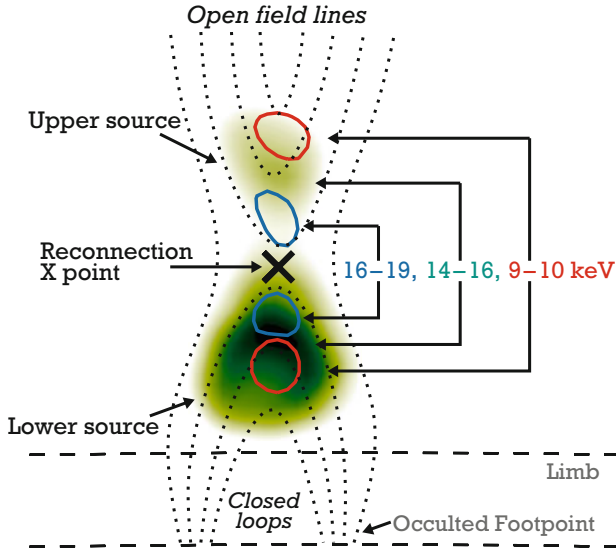
Fig. 12.5 Schematic diagram of the physical scenario superimposed on the RHESSI observations (contours at 9–10 and 16–19 keV) as a manifestation of the stochastic acceleration model. The dotted curves represent the magnetic field (Liu et al. 2008)

chromospheric footpoints. However, a thin-thick target model cannot account for the observed relations between the non-thermal spectra of coronal and footpoint sources (Battaglia and Benz 2007), while it is found to be consistent in partially occulted flares (Krucker et al. 2007b; Krucker and Lin 2008).

Superhot X-Ray sources ($T > 30$ MK) were detected in large coronal altitudes (even during the pre-impulsive flare phase), and thus are of coronal origin, rather than caused by chromospheric evaporation, which generally produces a high-temperature component of ≈ 20 MK also (Caspi and Lin 2010).

12.4   Modeling of Hard X-ray Spectra

Hard X-ray spectra from RHESSI have a high spectral resolution of ≈ 1 keV and allow us unambiguously to separate the thermal (exponential-like function) from the non-thermal (power law-like) spectral component, so that the thermal and non-thermal flare photons can be accurately separated (in photon space). However, there is one big problem that the low-energy cutoff of the nonthermal component (in particle energy space) cannot be easily determined. This low-energy cutoff is defined by the lowest energy where an electron can be accelerated out of the thermal distribution. The knowledge of this low-energy cutoff is necessary to avoid a singularity (and a huge over-estimate) of the extrapolated nonthermal spectrum

and related flux at the lowest energies. A correction term for the assumed *"cold-target"* energy loss in the thermal energy range eliminates the low-energy cutoff singularity (Emslie 2003). Spectral fitting with a broken power law function in terms of the thick-target model yields a low-energy cutoff varying between 20 and 40 keV during a large flare (Holman et al. 2003). A low-energy cutoff can be constrained by both hard X-ray and simultaneous microwave spectra (Holman 2003). Equipartition between thermal and nonthermal energy is found to be compatible with the data (Saint-Hilaire and Benz 2005). Sui et al. (2005) use a new method that combines spatial, spectral, and temporal analysis, based on the assumption that spiky time structures indicate non-thermal emission, while smooth time structures are expected for dominant thermal emission. A similar method was used based on analyzing the energy-dependent timing of thermal emission, where nonthermal hard X-ray emission shows extremely small electron time-of-flight delays in the order of $\lesssim$ 10–100 ms for nonthermal electrons, while thermal emission is controlled by conductive cooling and exhibits much larger delays in the order of a few seconds to a few tens of seconds. This method yields cross-over energies of $\epsilon_{th} = 18.0 \pm 3.4$ keV (where the hard X-ray spectrum transits from thermal to nonthermal emission), (Aschwanden 2007). These values can be considered as upper limits of the low-energy cutoff. A radically different approach to determine the low-energy cutoff was proposed by Kontar et al. (2015), based on a modification of the (warm) temperature regime due to chromospheric heating, evaporation, and turbulence, opposed to the standard cold-target model. The warm-target model of Kontar et al. (2015) has been applied to a large data set of solar flares, including 191 M- and X-class flares observed with AIA/SDO, which yields mean temperature of $T_e = 8.6$ MK in the thick-target region of flares, and a low-energy cutoff of $\epsilon_{wt} = 6.2 \pm 1.6$ keV (Aschwanden et al. 2016). The nonthermal energy exceeds the thermal energy in 85% of the events, which largely confirms the warm thick-target model of Kontar et al. (2015). As an alternative to the combination of thermal and nonthermal two-component spectra, a kappa distribution may be used instead, which has a Maxwellian-like core in addition to the power law tail, and has the nice feature that no assumption on the low-energy cutoff is required (Oka et al. 2013), but one should be aware that the kappa distribution is a mathematical convenience that is not derived from a physical model. Bain and Fletcher (2009) derived a physical model, but a specific velocity dependence is required for the energy diffusion in the acceleration region in order to obtain a kappa distribution.

Another effect of the thick-target model that needs to be included in fitting RHESSI hard X-ray spectra is the *non-uniform target ionization*. The decrease of ionization with depth in the atmosphere reduces long-range collisional energy losses and so enhances the hard X-ray bremsstrahlung efficiently there, elevating the high energy end of the hard X-ray spectrum by factors of up to 2.8 above that of an ionized target (Kontar et al. 2002). Evidence for such a spectrum was obtained by Su et al. (2011).

The spectral evolution of hard X-ray fluxes during impulsive solar flares was found to exhibit a correlation between the spectral index γ and the non-thermal flux

at 35 keV, which may be related to the generally observed soft-hard-soft evolution during the impulsive flare phase (Grigis and Benz 2004).

The effects of Compton backscattering were theoretically studied, where incoming photons become scattered in the dense chromosphere or photosphere, and this way contribute to a source broadening and to modified hard X-ray spectra (Massone et al. 2004; Saint-Hilaire and Benz 2005; Kontar et al. 2006, 2011; Kasparova et al. 2007). A major assumption in some backscattering models is the isotropy of the downward directed radiation (Kontar et al. 2006). Also, low-energy cutoffs inferred from mean electron spectra can sometimes be an artefact of the albedo (Kasparova et al. 2007).

The finite size of coronal hard X-ray sources has been investigated by forward-fitting of source visibilities in different energy bands, from which it was found that the average source sizes σ increase slowly with photon energy ϵ as $\sigma \propto \epsilon^{1/2}$ (Xu et al. 2008). This behavior is neither consistent with the predictions of a single-loop thermal model, nor with a model in which nonthermal electrons are injected into a constant-density structure from a compact acceleration region. On the other hand, it was concluded that the data are consistent with a nonthermal collisional model that incorporates an extended acceleration region (Xu et al. 2008), while other studies of the same flare events imply that hard X-rays come predominantly from the corona rather than from the more usual chromospheric footpoints (Dennis et al. 2018).

Fitting of hard X-ray spectra in a survey of partially occulted flares revealed that the coronal sources show faster time variations in the order of tens of seconds (than the thermal hard X-ray emission at $E \lesssim 15$ keV), which is likely to be thin-target emission in the corona from flare-accelerated electrons (Krucker and Lin 2008).

One generic model for hard X-ray emission is stochastic acceleration of particles by turbulence, where electrons accelerated at or very near the loop top produce thin-target bremsstrahlung emission there, and then escape downward producing thick-target emission at the loop footpoints. The model starts with the Fokker-Planck equation for the density spectrum of accelerated electrons, averaged over the turbulent acceleration region, includes the direct acceleration rate by turbulence, a particle diffusion rate, and a particle loss rate (by Coulomb collisions). Petrosian and Chen (2010) and Chen and Petrosian (2013) fitted this model to the 2003 November 3 flare and found an energy-dependence of the particle escape time T_{esc} scaling as,

$$T_{esc}(E) = 0.3 \text{ s} \left(\frac{E}{100 \text{ keV}} \right)^{\kappa}, \quad \kappa = 0.83 \pm 0.10 , \qquad (12.4.1)$$

and a scattering time τ_{scat}^{turb} due to turbulence,

$$\tau_{scat}^{turb}(E) = 0.016 \text{ s} \left(\frac{E}{100 \text{ keV}} \right)^{\lambda}, \quad \lambda = 1.90 \pm 0.14 . \qquad (12.4.2)$$

The energy-dependence of the escape time and the scattering time are shown in Fig. 12.6. Note that the escape time by turbulent scattering indicates a significantly
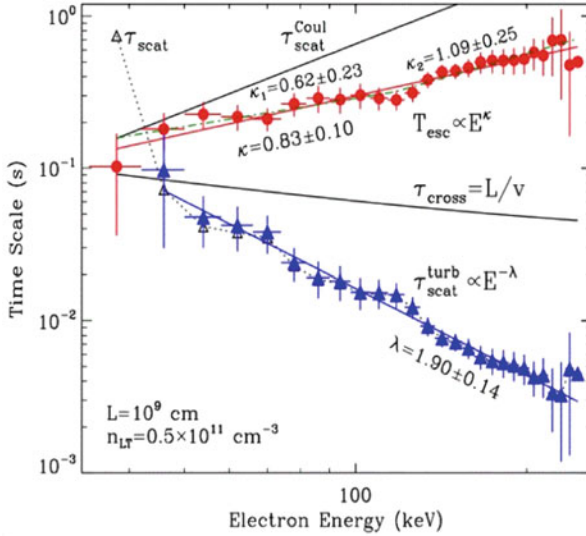
Fig. 12.6 Spectral modeling of the 2003 November 3 flare observed with RHESSI. The escape time (filled circles) and turbulence scattering time (filled triangles) in the loop top acceleration region are shown, both fitted with a power law dependence. The Coulomb collisional scattering rate $\tau_{scat}^{coul}(E) \propto E^{1.5}$ is shown in the top of the diagram (Petrosian and Chen 2010)

different scaling than what is expected for models with pure collisional Coulomb scattering (τ_{scat}^{Coul}), such as collisional trap models that have an escape time corresponding to the collisional deflection time (of scattering into the loss-cone),

$$\tau^{defl}(E) \approx 0.95 \text{ s } \left(\frac{E}{100 \text{ keV}} \right)^{3/2} \left(\frac{n_e}{10^{11} \text{ } cm^{-3}} \right)^{-1} \left(\frac{20}{\ln \Lambda} \right), \qquad (12.4.3)$$

with $\ln \Lambda$ being the Coulomb logarithm. Other statistical studies found that the energy-dependent time delays of $\approx$ 20–200 keV hard X-ray emission is consistent with the weak-diffusion limit (e.g., Aschwanden et al. 1997), opposed to the result of significant turbulent scattering in the 2003 November 3 flare modeled by Petrosian and Chen (2010), but the authors point out that this result may not be representative of typical flares, which have generally softer spectra for the loop top sources.

12.5 Rapid Magnetic Changes During Flares

Since magnetic reconnection dissipates part of the local magnetic energy during flares, the non-potential magnetic energy, or the free energy (i.e., the difference between the non-potential and potential magnetic energy) is expected to be reduced during a flare. Potential fields are stable because they represent the lowest state

of energy and cannot be dissipated by a magnetic reconnection process. Earlier studies describe rapid changes of magnetic fluxes associated with flares, without distinguishing between potential and non-potential magnetic field components (Wang et al. 2002; Yurchyshyn et al. 2004), while more recent studies quantify the fraction of dissipated free energy (e.g., Schrijver et al. 2008; Sun et al. 2012; Aschwanden et al. 2014).

Analyzing the line-of-sight component B_z of 6 X-class flares it was found that they all had an increase in the magnetic flux of the leading polarity of order of a few times 10^{20} Mx, while each event exhibited a permanent decrease in the magnetic flux of the following polarity (Wang et al. 2002; Yurchyshyn et al. 2004). The fact that the magnetic changes are permanent proves that they are due to an irreversible change in the reconnection topology, and not due to a reversible disturbance during a flare. The penumbral fields change from a highly inclined to a more vertical configuration, which leads to penumbral decay (Liu et al. 2005). Rapid changes in the magnetic gradient occurred in each of the analyzed events, corresponding to a magnetic gradient increase for converging motions, and to a gradient decrease for diverging motions (Wang 2006).

Using *Global Oscillation Network Group (GONG)* magnetograms in a statistical study of 15 X-class flares it was found that 75% of the locations exhibited flare-associated magnetic field changes within less than 10 min of the flare start, in a range of $B \approx 30$–300 G, while the changes corresponded to a decrease in two-thirds of the cases (Sudol and Harvey 2005).

Possible explanations for the rapid magnetic flux changes were proposed in terms of (i) the emergence of very inclined flux loops, (ii) a re-orientation of the magnetic field direction, (iii) expansion of the sunspot with less Zeeman saturation, or (iv) relaxation of penumbral fields by upward reconnecting magnetic fields above the photosphere (Wang et al. 2002; Yurchyshyn et al. 2004, Sudon and Harvey 2005). Combining the findings it became clear that magnetic reconnection plays a role in all cases. When an active region is away from the solar disk center, the reconnected transverse fields cause an apparent increase of the flux in the polarity towards the limb, and a decrease for the polarity closer to the disk center (Wang 2006).

The Lorentz force per unit area in the vertical direction,

$$\delta F_z = \frac{1}{4\pi} \left(B_z \delta B_z - B_x \delta B_x - B_y \delta B_y \right) \tag{12.5.1}$$

has been calculated from *Big Bear Solar Observatory (BBSO)* magnetograph data, which confirmed that the photospheric magnetic field responds to coronal field restructuring, and that the photospheric magnetic field near the polarity inversion line becomes more horizontal, as expected for the newly formed low-lying fields resulting from tether-cutting reconnection (Wang and Liu 2010; Wang et al. 2012; Petrie 2013). A detailed model of the Lorentz forces acting during the abrupt magnetic changes of the X2.2 flare is presented in Petrie (2013), while the Lorentz-force method applied to other flares is discussed in Petrie (2014).

Nonlinear force-free magnetic field (NLFFF) modeling of solar flares was conducted with Hinode/SOT vector magnetic field data and 14 NLFFF codes, revealing strong electrical currents that emerge together with the magnetic flux before a flare in a large-scale twisted flux rope topology, liberating a free magnetic energy of $\approx 10^{32}$ erg during a X3.4 GOES-class flare (Schrijver et al. 2008). It was concluded that (i) strong electrical currents emerge together with magnetic flux preceding the flare, (ii) that these currents are carried in an ensemble of thin strands, (iii) that the global pattern of these currents and field lines are compatible with a large-scale twisted flux rope topology, and (iv) that the magnetic energy change of $\Delta E \approx 10^{32}$ erg is sufficient to power the X3.4 flare and its associated CME (Schrijver et al. 2008).

The evolution of the magnetic field during major eruptive flares exhibits fast magnetic flux emergence (over 5 days) and strong shearing motion, leading to a quadrupolar sunspot complex that produced several major eruptions, including the first X-class flare (2011 February 14) of Solar Cycle 24 (Fig. 12.7). Magnetic (NLFFF) modeling yields free energies of $\approx 2.6 \times 10^{32}$ erg (Sun et al. 2012). During the flare, the photospheric field changes rapidly: the horizontal field was enhanced by 28% in the core region, and it becomes more inclined and more parallel to the polarity inversion. The flare-associated changes in the magnetic field were found to be consistent with the coronal "implosion" or tether-cutting reconnection model (Sun et al. 2012; Liu et al. 2012).

NLFFF modeling in a major statistical study of ≈ 400 M- and X-class flares using AIA/SDO and HMI/SDO data was performed with the goal to determine the potential energies E_P, the non-potential energies E_{NP}, the free energies $E_{free} = E_{NP} - E_P$, and the fraction of dissipated magnetic energies E_{diss} during flares, based on the difference of the free energy before and after the flares (Aschwanden et al. 2014). The underlying NLFFF model was based on the *vertical current approximation (VCA-NLFFF)*, which produces energy decreases by untwisting of helical (sigmoidal) coronal field lines. The free energies varied in the range of $E_{free}/E_p \approx 1\%-25\%$, and the flare-dissipated energies amount to a substantial fraction of the free energy with a scaling of $E_{diss} \propto E_{free}^{0.9}$. A study of flare-rich but CME-poor active regions revealed that confined flares may leave weaker photospheric and coronal imprints of rapid magnetic changes than their eruptive counterparts (Sun et al. 2015).

Variations of the magnetic field may be caused even in the preflare phase, detectable as preflare brightenings, or as opposite-polarity magnetic flux elements, where the magnetic orientation of small bipoles is opposite to that of the ambient main polarities (Wang et al. 2017; Xu et al. 2017).

First detections of chromospheric magnetic field changes during an X1-class flare were made with IBIS Ca II 8542 Å by Kleint (2017). Photospheric magnetic changes are predominantly located near a polarity inversion line, and chromospheric changes occur near the footpoints of loops (Kleint 2017).
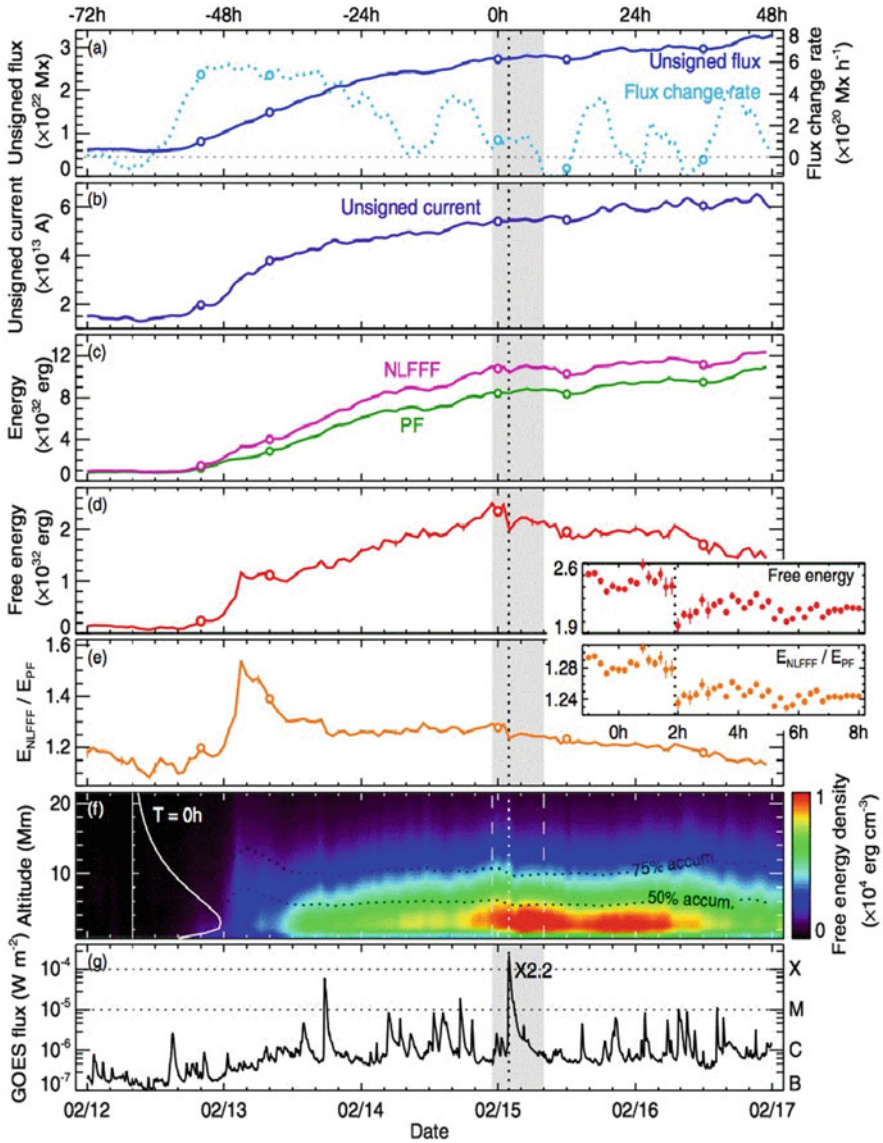
Fig. 12.7 Evolution of magnetic energy and related quantities of active region NOAA 11158 over 5 days (2011 February 12–17): (**a**) Total unsigned magnetic flux and flux change rate, (**b**) total unsigned current, (**c**) non-potential and potential field energy, (**d**) free energy, (**e**) ratio of nonpotential to potential energy (with insert for the X2.2 flare), (**f**) time-altitude diagram of average magnetic free energy density, and (**g**) GOES soft X-ray flux (1–8 Å), (Sun et al. 2012)

12.6   Magnetic Reconnection and Particle Acceleration

From magnetospheric in-situ measurements, laboratory experiments, analytical and numerical models, it is well known that particles are accelerated near the X-points in DC electric fields associated with magnetic reconnection (Drake et al. 2006; Chen et al. 2008; Che et al. 2011). If a reconnection process has multiple X-points, which is a characteristic of the secondary tearing-mode and coalescence instability, also known as *bursty reconnection mode*, the multitude of X-points strongly enhances the number of accelerated particles and their maximum energy, in comparison to single X-point reconnection (Kliem et al. 2000). The *impulsive bursty reconnection regime* produces plasmoids intermittently, by tearing and coalescence of magnetic islands near X-points, and this way modulates the local electric field at X-points, filamentary electric currents, the rate of accelerated (nonthermal) particles, and the associated fluxes observed in bursty hard X-ray emission and in quasi-periodic decimetric radio emission (Kliem et al. 2000). The energy spectra of accelerated particles during multi-island magnetic reconnection have been derived to have a power-law distribution function $\propto E^{-1.5}$ (Drake et al. 2013).

Magnetic reconnection at an X-point appears to be driven by lateral inflows and longitudinal outflows of plasma, where the particles become re-organized in the local diffusion region of vanishing anti-parallel magnetic fields. The first evidence of reconnection inflow in a solar flare was inferred from EUV observations of an X-point (visible in form of a cusp) with plasmoid ejection, formation of magnetic islands, and lateral inflow motions with a speed of $v \approx 5\,\mathrm{km\,s^{-1}}$, which corresponds to a reconnection rate or Alfvén Mach number of $M_A = 0.001$–0.03 (Yokoyama et al. 2001). Simultaneous observations of reconnection inflows and outflows were identified in the 2010 August 18 flare, with inflow speeds of $v_{in} = 12$–$90\,\mathrm{km\,s^{-1}}$ and outflow speeds of $v_{out} = 220$–$280\,\mathrm{km\,s^{-1}}$ (Takasao et al. 2012).

The spatial structure of the bursty reconnection mode is thought to be fractal, but continuously driven by ejection of (fractal) plasmoids, also called *plasmoid-induced reconnection in a fractal current sheet* (Shibata and Tanuma 2001). The initial plasmoid ejection was already part of the standard CSHKP flare model. The fractal structure of the current sheet is thought to occur with the following chain reaction: primary tearing, sheet thinning, Sweet-Parker current sheet, secondary tearing, further sheet thinning, etc. (Fig. 12.8). These processes occur repeatedly at smaller scales until a microscopic scale (either the ion Larmor radius or the ion inertial length) is reached where anomalous resistivity or collisionless reconnection occurs. The current sheet eventually has a fractal structure with many plasmoids, magnetic islands, and X-points of various sizes (Shibata and Tanuma 2001). The first relaxation episode after the initial thinning and (primary) tearing instability can explain the initial downward motion of the flare hard X-ray source before the hard X-ray source gradually moves upward (Sui et al. 2004; Ji et al. 2008), which is also called the *collapsing trap* (Veronig et al. 2006). The initial downward motion may also create large-scale Alfvén wave pulses and turbulent cascades, which can accelerate particles in the denser low-altitude regions and ameliorate the
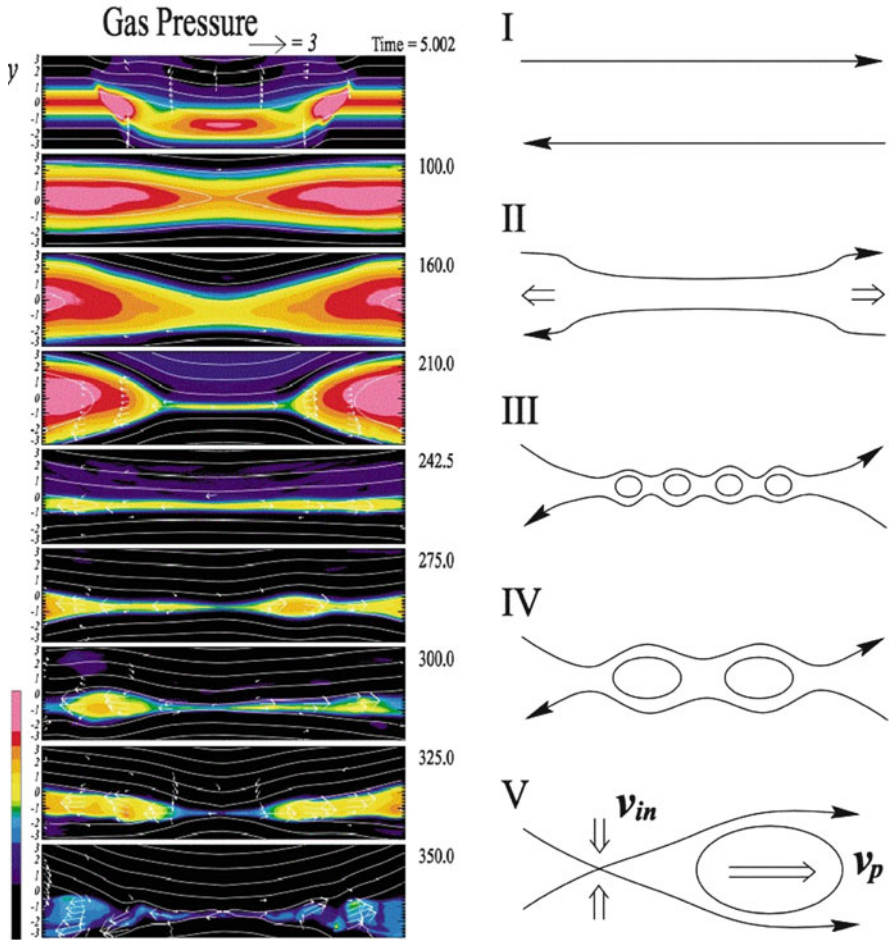
Fig. 12.8 *Right:* The scenario of plasmoid-induced reconnection in a fractal current sheet, which involves: The initial current sheet (I), current sheet thinning and evolution into Sweet-Parker sheet (II), secondary tearing of Sweet-Parker sheet (III), coalescence of magnetic islands (IV), and ejections of plasmoids (V). *Left:* Numerical simulation of the same scenario with time evolution (from top to bottom panel), where the color scale corresponds to the gas pressure, (Shibata and Tanuma 2001)

number problem (Fletcher and Hudson 2008). However, particle acceleration near the footpoints of flare loops disagrees with electron time-of-flight measurements (Aschwanden et al. 1996).

The magnetic field configuration during the reconnection process was found to have a sigmoid structure (Ji et al. 2008; Zhao et al. 2016; Li and Zhang 2015), an X-shaped ribbon structure (Li et al. 2016), a sheared arcade that evolved into a less sheared postflare arcade (Aulanier et al. 2012), a fan-spine magnetic

topology (Sun et al. 2013), J-shaped ribbons (Janvier et al. 2014), hooked flare ribbons (Zhao et al. 2016), or quasi-separatrix layers (Aulanier et al. 2006; Janvier et al. 2013, 2016; Dudik et al. 2014; Zhao et al. 2016). A further class of magnetic configurations are δ-sunspots, which have been broken down into the 4 categories of spot-spot, spot-satellite, quadrupole, and inter-active region cases (Toriumi and Takasao 2017; Toriumi et al. 2017).

The electric field E_c in reconnecting current sheets has been inferred during flares in terms of the Lorentz force, i.e., $E_c = v_\parallel B_n$, exerted by the horizontal flare footpoint motion $v_\parallel$ and the normal component of the magnetic field B_n, yielding a footpoint motion of $v_\parallel \approx 20$–100 km s^{-1} and an electric field of $E_c \approx 90$ V cm^{-1} (Qiu et al. 2002). Correlations between the hard X-ray flux and the upward motion were found, which confirmed the theoretically expected relationship between the reconnection rate and the flux of accelerated electrons (Sui et al. 2004).

Evidence for the X-point structure of magnetic reconnection in flares has been provided by the observation of double hard X-ray sources symmetrically located above and below a coronal X-point (Sui and Holman 2003; Liu et al. 2008, Sect. 12.3)

The time evolution of *bursty reconnection* is highly intermittent and dynamic, which has also been modeled with a *slipping magnetic reconnection* scenario in *quasi-separatrix layers (QSL)*, where successive reconnection occurs that is seen as an apparent "flipping" or "slipping" motion (Aulanier et al. 2006; Janvier et al. 2013, 2016; Dudik et al. 2014; Li and Zhang 2015).

12.7   Microflares and Nanoflares

The size distribution of flares extends from maximum values of $E \lesssim 10^{33}$ erg down to $E \gtrsim 10^{24}$ erg, which covers about 9 orders of magnitude (Fig. 6.14; Aschwanden et al. 2000b). Small-sized flares with an energy range of 10^{27}–10^{29} erg, the smallest events that are detected in hard X-ray wavelengths, are also called *microflares*, while even smaller events are named *nanoflares*. RHESSI registered hard and soft X-rays from over 25,000 microflares (Christe et al. 2008; Hannah et al. 2007, 2008, 2010, 2011; Stoiser et al. 2007), which were found to be distributed evenly in the northern and southern mid-latitude band (Fig. 12.9), and all are associated with active regions, and thus they are very important for understanding the heating of active regions, which may be different from the heating of the corona in *"Quiet Sun"* regions (Sect. 6.8)

Some early statistics of nanoflares/microflares in Quiet Sun regions has been gathered from analyzing images in EUV wavelengths with the *EUV Imaging Telescope (EIT)* onboard SOHO, yielding a power law distribution of $N(E) \propto E^{-\alpha}$, with power law slopes of $\alpha \approx 2.3$–2.6, in the energy range of $E \approx 8 \times 10^{24}$–$1.6 \times 10^{26}$ erg (Krucker and Benz 1998). It was concluded that the extrapolation of the same power law slope down to energies of 3×10^{23} erg would constitute sufficient
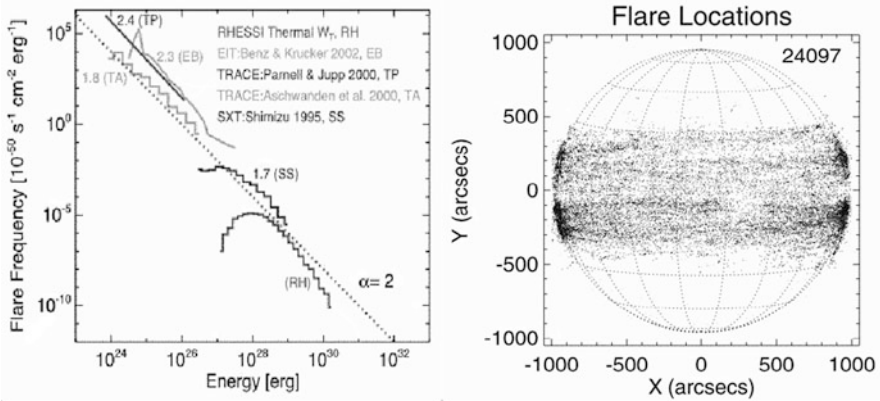
Fig. 12.9 *Left:* Synthesis of frequency distributions of the thermal energy of 8161 RHESSI microflares (RH) in the context of thermal energy distributions of nanoflares (TA, TP, and EB) and active region transient brightenings (SS). The dotted line indicates a power-law index of $\alpha = 2$. *Right:* Flare locations of 24,097 microflares detected with RHESSI, which spread over the two low-latitude bands. Note that the (centroid) locations have all a very low coronal height (Hannah et al. 2008; Christe et al. 2008)

energy to match the coronal heating requirement in the Quiet Sun (Krucker and Benz 1998), but the extrapolation of the power law size distribution to unobserved energies is questionable (Benz and Krucker 2002), especially for power law slopes above the critical value $\alpha \geq 2$, where the size distribution diverges at the low end (Hudson 1991). From multi-wavelength observations of small heating events in the Quiet Sun, using EIT/SOHO, CDS/SOHO, and the *Very Large Array (VLA)* in centimeter wavelengths, it was established that heating events with thermal energies of $\approx 10^{26}$ erg share many common thermal and non-thermal characteristics of larger flares, and thus they can be considered as miniature versions of regular flares, with an energy size corresponding to microflares (as detected in hard X-rays earlier) or large nanoflares (Krucker and Benz 2000).

Nanoflare statistics in the Quiet Sun was then obtained with the *Transition Region And Coronal Explorer (TRACE)* instrument, which had a pixel size of $0.5''$ that was three times smaller than EIT ($1.59''$), which yielded energy size distributions in the range of $E \approx 10^{24}$–10^{26} erg (Parnell and Jupp 2000; Aschwanden et al. 2000b). Although the energy estimates were compatible with data from EIT and TRACE, the power law slope of the size distributions differed significantly, being $\alpha \approx 2.3$–2.6 for EIT (Krucker and Benz 1998), $\alpha \approx 2.4$–2.6 (Parnell and Jupp 2000) or $\alpha \approx 1.8$ (Aschwanden et al. 2000b) for TRACE, a mismatch that resulted from different assumptions of the geometric flare volume model, incomplete temperature coverage, event detection thresholds, and event selection methods (Aschwanden et al. 2000a,b; Benz and Krucker 2002). Nevertheless, the best-fitting size distribution that is consistent with nanoflare statistics in EUV and

microflare statistics in soft X-rays was found to scale as (Aschwanden et al. 2000b),

$$N(E) \approx 10^{-46} \left(\frac{E}{10^{24} \text{ erg}} \right)^{-1.8} \qquad \text{s}^{-1} \text{ cm}^{-2} \text{ erg}^{-1} . \qquad (12.7.1)$$

which is shown in Fig. 6.14. Heating events in the picoflare regime $E \approx 10^{21}$–10^{24} erg were found to be implausible, because the scaling laws of the flare area, flare temperature, flare density, and chromospheric height extrapolated to these lower energies violate physical conditions that are conducive to coronal heating (Aschwanden et al. 2000b). Further studies on nanoflare statistics improved on the fractal geometry of nanoflares and on more complete temperature coverage (combining EUV data from TRACE with soft X-ray data from Yohkoh), yielding fractal Hausdorff dimensions of $D = 1.5 \pm 0.2$ and flatter size distributions of the thermal energy with a power law slope of $\alpha = 1.54 \pm 0.11$ (Aschwanden and Parnell 2002).

Since the coronal heating problem remained undecided after the controversial results of nanoflare statistics in EUV and soft X-ray wavelengths, the search for a hot component in microflares (using RHESSI data) continued. Open-shutter RHESSI observations of 3–15 keV X-rays revealed active region brightenings with a thermal component of $T = 6$–14 MK, which dominates in the 3–9 keV energy range and was interpreted in terms of beam-driven evaporation (Benz and Grigis 2002). Hard X-ray microflares were detected down to 3 keV, corresponding to the GOES-class level of B6 to A6, which exhibited a non-thermal component down to $\approx$ 6–7 keV, with energies of 10^{26}–10^{27} erg, and steep power law slopes of $\gamma \approx$ 5–8 (Krucker et al. 2002). Systematic studies of microflares detected by RHESSI yielded temperatures of $T \approx$ 11–15 MK, which are likely to be biased towards too high values, because they fit the high-temperature tail of the *differential emission measure (DEM)* distributions only and because RHESSI is not sensitive to emission measures at lower temperatures (Stoiser et al. 2007), a bias that affects also other published results as comparisons between GOES and high RHESSI temperatures demonstrate (e.g., Battaglia et al. 2005; Ryan et al. 2014; Hannah et al. 2008; McTiernan 2009; Reale et al. 2009).

RHESSI provided also the first limits on the 3–200 keV X-ray spectrum of the Quiet Sun, using a newly developed chopping technique (fan-beam modulation) during seven off-pointing periods during 2005–2006, when the GOES level was down to a background flux of 10^{-8}–10^{-7} W m^{-2}. These lower limits at 3–6 keV correspond to coronal temperatures of $T \leq 6$ MK and can even be used to estimate the axion-to-photon coupling constant or cosmic ray effects (Hannah et al. 2007, 2010).

Large statistics of RHESSI-detected microflares have been undertaken, yielding 25,705 microflares during the years of 2002–2007, using an automated flare-finding algorithm in the 6–12 keV energy range (Christe et al. 2008). The main microflare duration is $\approx$ 6 min, the time-averaged energy is $\lesssim 10^{26}$ erg, and the peak count rate size distributions show power law slopes of 1.50 ± 0.03 at 3–6 keV, or a

range of 1.50–1.58 for different energy ranges and years (Christe et al. 2008). Statistical distributions of thermal and nonthermal energies, emission measures, and temperatures of RHESSI-detected microflares are presented in Hannah et al. (2008), which demonstrate that they fit a natural extension of the size distributions of nanoflares and active region brightenings, in the energy range of $E = 10^{27}$–10^{30} erg (Fig. 12.9). See also Hannah et al. (2011) for a review on microflare statistics.

Evidence for nonthermal particles in coronal microflares, hypothetically being heated impulsively by Parker-type nanoflares, was sought by analysis of chromospheric brightenings in *Interface Region Imaging Spectrograph (IRIS)* data, which revealed small events with rapid variability ($\approx$ 20–60 s) of intensity and velocity on small spatial scales of $\lesssim$ 500 km, and blueshifted components (Testa et al. 2014; Polito et al. 2015; Young et al. 2015). Numerical simulations with the RADYN code can reproduce small heating events with thermal energies of $E \approx 6 \times 10^{24}$ erg, produced by electron beams that penetrate into the transition region (Testa et al. 2014), but it is not clear whether those events correspond to the microflares detected by RHESSI. Similarly small flares ($\lesssim$ 500 km) were observed also with the 1.6-m *New Solar Telescope (NST)* (Jing et al. 2016).

12.8   Flare Hard X-Ray Oscillations

There are two basic types of oscillations: (i) Resonance phenomena or normal modes (with eigen-values), such as a standing MHD wave, and (ii) *nonlinear limit cycles*, which are manifestations of self-organizing systems, where a driving force is counteracted by a negative feedback force. The two types of oscillations can be distinguished by their degree of periodicity, i.e., MHD waves generally show a strict periodicity (although often with a damped oscillation amplitude), while nonlinear limit cycles are quasi-periodic (with occasional glitches). The physical mechanism of an oscillator system needs to be identified indirectly, while the detection of oscillations is generally faciliated by a secondary (radiation) mechanism, such as free-free bremsstrahlung in hard X-ray wavelengths, or plasma emission and gyrosynchrotron emission in radio wavelengths. While numerous observations of oscillations were reported earlier, much progress in the new millennium has been made from imaging observations in many wavelengths (for reviews see Aschwanden 1987; Nakariakov and Melnikov 2009).

A sequence of 4 periodic pulses with a period of $P = 6.6$ s was detected during a flare with the *Hard X-ray Telescope (HXT)* onboard Yohkoh in three energy bands between 14 keV and 53 keV, as well as with the *Nobeyama Radio Heliograph (NoRH)* (Asai et al. 2001). Because the period is close to the Alfvén transit time along the flare loop, it was concluded that the number of accelerated electrons is modulated by macroscopic magnetic structures, such as MHD oscillations in flare loops (Asai et al. 2001).

First high-resolution imaging observations of *quasi-periodic pulsations (QPP)* during flares were obtained from RHESSI (3–25 keV), from which evidence for the

presence of a trans-equatorial loop with kink-mode MHD oscillations was obtained (Foullon et al. 2005). The QPPs were interpreted as periodic pumping of electrons in a compact flaring loop, modulated by oscillations in a magnetically linked and larger loop acting as a long-period MHD resonator, for the 2004 February 5–6 flare with a loop length of $L \approx 500$–600 Mm, periods of $P = 8$–12 min, and Alfvénic phase speeds of $v_{ph} = 2L/P = 1400$–2500 km s^{-1} (Foullon et al. 2005). QPP events can be subdivided into a long-periodic class where an external large-loop resonator is involved, and into a short-periodic class that contains single-loop fast kink-mode MHD oscillations (Foullon et al. 2010).

A considerable number of flare pulsation events in hard X-rays were reported from RHESSI observations (P=480–720 s, Foullon et al. 2005; P=240 s, Dauphin et al. 2005; P=120–240 s, Ofman and Sui 2006; P=227–280 s, Li and Gan 2008; P=16 s, Inglis et al. 2008; P=14.5–18.4 s, Fleishman et al. 2008; P=15, 36 s, Zimovets and Struminsky 2010; P=600–1080 s, Foullon et al. 2010; P=1–30 s, Dolla et al. 2012; P=25–120 s, Ning 2014; P=8–270 s, Kuznetsov et al. 2016; P=180 s, Kumar et al. 2016). An interpretation in terms of a physical model that fits the data with a unique solution could often not be established. Observational constraints include not only the periods, densities, temperatures, and magnetic fields, but also the microwave modulation depth, the spectral index of optically thin radio emission, the degree of circular polarization, and the electron pitch-angle distribution (Fleishman et al. 2008). Double-periodic emission was detected ($P_1 = 16$ s, $P_2 = 36$ s), which was attributed to MHD oscillations in two spatially separated, but interacting systems of flaring loops (Zimovets and Struminsky 2010).

For the > 25 keV quasi-periodic oscillations of the 2005 January 19 flare it was suggested that the oscillations are due to variations of the current magnitude in the reconnection region, induced by Alfvénic or super-Alfvénic beams. The electric current fluctuations modulate the electric field magnitude, and consequently modulate the electron acceleration and associated thick-target hard X-ray emission (Ofman and Sui 2006).

Besides RHESSI, quasi-periodic pulsations of hard X-ray or gamma-ray emission was also detected with *WATCH/Granat* (P=143.2±0.8 s, Terekhov et al. 2002); with the *Hard X-ray Spectrometer (HXRS)* onboard the *Energy Multi-Spectral Thermal Imager (MTI)* (P=25–48 s, Farnik et al. 2003); with SONG/CORONAS-F (P=40 s, Nakariakov et al. 2010), with HXT/Yohkoh (Jakimiec and Tomczak 2010, 2012), with the *Fermi Gamma-Ray Burst Monitor (GBM)* (Gruber et al. 2011; Li et al. 2015; with the *Euv Spectro Photometer (ESP)* onboard SDO and the *Project of On-Board Autonomy (PROBA)* (Dolla et al. 2012); The detection of quasi-periodic pulsations in solar flare gamma-rays was disputed for data that are governed by red-noise (Gruber et al. 2011).

The modulation of quasi-periodic hard X-rays has also been interpreted in terms of magnetic trapping in the temporary cusps above flare loops where X-type reconnection occurs according to standard flare models. During the compression of an oscillating magnetic trap, particles are accelerated, while chromospheric
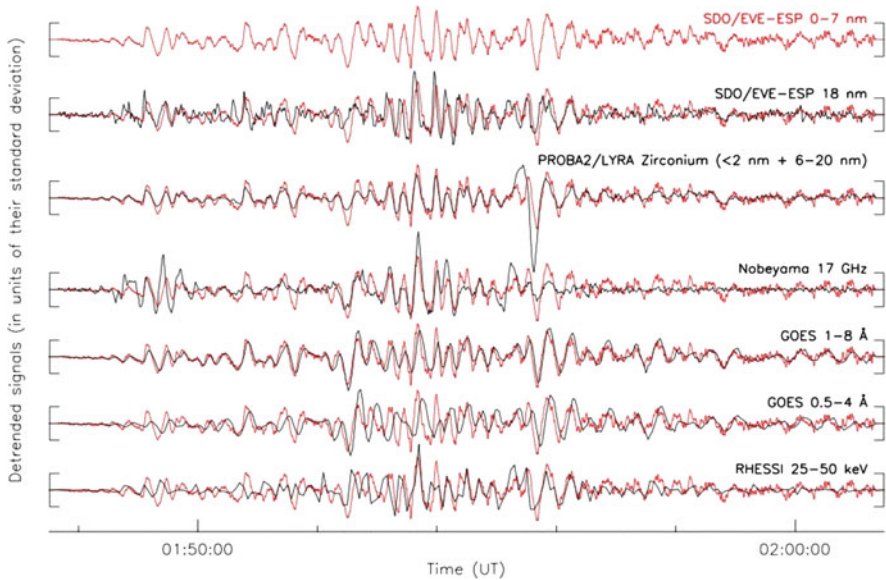
Fig. 12.10 Normalized time profiles of different instruments during the 2011 February 15, X2.2 flare. The time profiles are detrended by subtracting a signal that is smoothed with a 20 s boxcar. The ESP0–7/SDO light curve (red) is overplotted on each curve for comparison (Dolla et al. 2012)

evaporation fills the trap and quenches particle acceleration (Jakimiec and Tomczak 2010, 2012), leading to a quasi-periodic nonlinear limit cycle between the two competing processes.

The 2011 February 15 (GOES X2.2-class) flare was observed with many instruments (ESP/AIA, PROBA, GOES, NoRH), where a time lag of $\approx$ 9 s was measured between EUV and soft X-ray pulsations (Fig. 12.10). This was interpreted in terms of the time difference between the directly-precipitating electrons and the trapped electrons (with larger pitch angles) that are scattered into the loss-cone after a collisional deflection time, before they produce bremsstrahlung in hard X-rays (Dolla et al. 2012). The relative time delays, however, are subject to corrections due to a later revision of the GOES time stamps (Dolla, private communication). Although pulsations in hard X-rays and UV are often well-correlated temporally, the detailed spatial evolution of UV ribbons and hard X-ray sources is not understood (Inglis and Gilbert 2013).

One observation of quasi-periodic pulsations has been interpreted as a two-ribbon flare with subsequent reflections of slow waves that propagate in up and downward direction (Nakariakov and Zimovets 2011), which has been disputed by Inglis and Dennis (2012), because no correlation between the hard X-ray footpoint separation and the pulse timing was found.

Analyzing quasi-periodic pulsations from both gamma-rays (GBM/Fermi) and chromospheric Doppler velocities (with IRIS) leads to the conclusion that QPPs are

produced by non-thermal electrons that are accelerated by induced quasi-periodic magnetic reconnection in a flare (Li et al. 2015; Hayes et al. 2016). The observations are consistent with a series of energy injections by nonthermal particle beams into the chromosphere (Brosius et al. 2016).

A systematic analysis of 29 hard X-ray flares with quasi-periodic pulsations in the 50–100 keV range suggests that an eruptive flux rope can act as a trigger of the pulsating flare energy release (Kuznetsov et al. 2016).

In one case a 3-min QPP was observed that was highly correlated with the 3-min oscillations in a nearby sunspot (Kumar et al. 2016). It was suggested that the periodic reconnection (modulated either by a sunspot slow-mode wave or by an untwisting filament) at a magnetic null point most likely causes the repetitive particle acceleration.

QPPs in hard X-rays can also be detected from the time derivative of the GOES soft X-ray light curves. For instance, the X3.2 flare on 2013 May 14 reveals a total of 163 distinct pulses over a duration of 2 hours (Dennis et al. 2017).

12.9   Flare Radio Emission

Solar radio bursts are usually subdivided into coherent and incoherent emission mechanisms. Incoherent mechanisms (such as free-free bremsstrahlung, gyro-emission, or gyro-synchrotron emission) are additive, in the sense that the number of emitted photons is linear to the volume in which they are emitted. Coherent radio emission, in contrast, is multiplicative, in the sense that they have a nonlinear scaling between the observed flux and the emitting volume. Coherent radio bursts undergo some resonant wave-particle interaction process that displays exponential growth during some time interval, driven by some unstable anisotropic particle distribution (in momentum and pitch angle space), such as the (bump-in-tail) beam instability (giving rise to type III bursts), or the loss-cone instability (producing quasi-periodic decimetric oscillations or electron cyclotron maser spikes). The physical mechanisms of solar radio bursts are difficult to pin down by remote-sensing observations, but some progress occurred by identifying the underlying instabilities using new multi-frequency imaging data. For recent reviews see Benz et al. (2005), Chernov (2006), Nindos et al. (2008), and White et al. (2011).

Statistics of radio fluxes, spectral peaks, and spectral slopes have been obtained from 412 solar radio bursts observed during 2001–2002 at 40 frequencies in the 1.2–18 GHz range with the *Owens Valley Solar Array (OVSA)* (Nita et al. 2004). A survey of radio emission during 201 selected X-ray solar flares in the frequency range of 100 MHz to 4 GHz was carried out with the *Phoenix-2 spectrometer* of ETH Zürich, which yielded the following morphological burst types: type III's, pulsations, diffuse continua, narrowband spikes, type IV bursts, and high-frequency broadband (gyro-synchrotron) bursts (Benz et al. 2005). A survey of solar radio bursts with drifting (zebra-like) stripes in emission and absorption offers two possible interpretations: (i) interactions between electrostatic plasma

waves and whistlers, and (ii) radio emission at the *double plasma resonance (DPR)* (Chernov 2006). Standing and propagating sausage-mode oscillations are expected to modulate the DPR layers differently, which could be used as a diagnostic (Yu et al. 2016).

Both microwave and hard X-ray spectra are sensitive to low- and high-energy cut-offs of the electron distribution function. The optically thick portion of a microwave spectrum is enhanced and smoothed by a low-energy cutoff, while a hard X-ray spectrum is flattened below the cutoff energy. The determination of the high-energy cutoff from these spectra establishes the highest electron energies produced by the acceleration mechanism, while determination of the low-energy cutoff is crucial for establishing the total energy in accelerated electrons (Holman 2003). Joint modeling of microwave and hard X-ray spectra suggests a break point of the electron spectra at a few hundred keV, and harder spectra at higher energies that contribute to microwave gyro-synchrotron emission (Asai et al. 2013). Modeling of the gyro-synchrotron emission of an impulsive, but X-ray-poor impulsive flare (Fig. 12.11; Bastian et al. 2007), indicated the absence of chromospheric evaporation, and possibly a large magnetic mirror ratio that disables electron trapping (Bastian et al. 2007).

From microwave imaging with the *Nobeyama Radio Heliograph (NoRH)* at frequencies of 17 and 34 GHz (gyro-synchrotron emission), an initial shrinkage of radio flare loops was observed (Li and Gan 2005), which corresponds to the initial downward motion of coronal flare loops seen in soft and hard X-rays (Sect. 12.3).
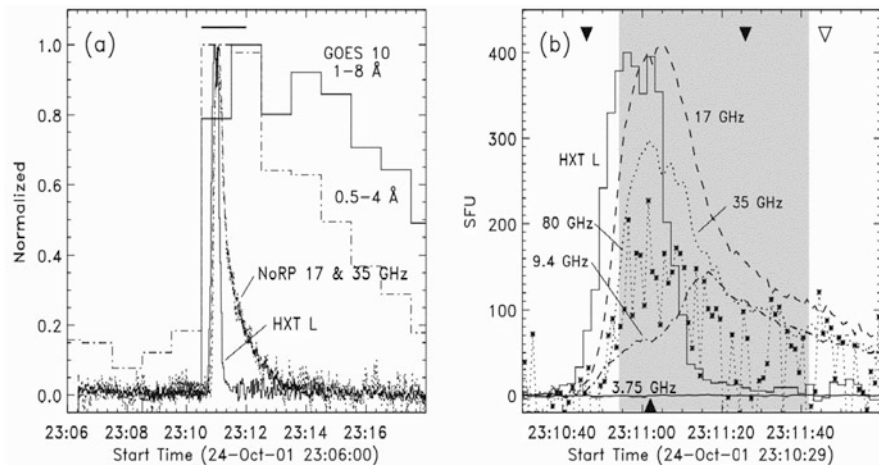
Fig. 12.11 Time profiles of the 2001 October 24, 23:11 UT, flare. (**a**) Nobeyama Radio Heliograph (NoRH 17 and 35 GHz), GOES (1–8, and 0.5–4 Å), HXT/Yohkoh L-band 13.9–22.7 eV. (**b**) Detail of the NoRP (17 and 35 GHz) and HXT L observations, with additional data from the *Owens Valley Solar Array (OVSA)*, (3.75, 9.4, 80 GHz, and *TRACE 171 Å* (histogram), Bastian et al. 2007)

Quasi-periodic decimetric radio emission in the frequency range of $\nu = 0.6$–2 GHz during the flare of 1992 October 25, 09:25 UT, has been interpreted in terms of a dynamic magnetic reconnection scenario. Quasi-periodic particle acceleration episodes are thought to result from dynamic processes in a large-scale current sheet, where reconnection is dominated by repeated formation and subsequent coalescence of magnetic islands (known as "secondary tearing" or "impulsive bursty" regime of reconnection), while a continuously growing plasmoid is fed by newly coalescing islands (Fig. 12.8, Kliem et al. 2000). 2-D MHD simulations reproduce bursty or quasi-periodic electric currents at the main X-points of Petschek-like reconnection. Related studies focus on the reconnection of a kinking flux rope that triggers the ejection of a microwave and hard X-ray plasmoid (Kliem et al. 2010; Karlicky and Kliem 2010), or on electromagnetic emission generated by Langmuir waves during a coalescence of plasmoids (Karlicky et al. 2010; Karlicky and Barta 2011).

Quasi-periodic broadband radio emission was observed during the 2003 June 15 flare, for which a model with quasi-periodic acceleration and injection of fast electrons was found to be fit the observed modulation and spectra better than a model with MHD oscillations (Fleishman et al. 2008). The 1998 May 8 flare, which showed quasi-periodic pulsations in microwave (17 GHz) and soft X-ray wavelengths, was found to be consistent with the interpretation of sausage-type MHD oscillations which periodically modulate the flare loop cross-section and magnetic field (Inglis et al. 2008). Except for this particular event, the prevalence of oscillatory signals in other solar flares was questioned, based on a Bayesian analysis of power law-like Fourier power spectra of hard X-ray and microwave data (Inglis et al. 2015). An alternative way to analyze periodic signals was attempted with the *Hilbert-Huang transform* applied to an *ensemble empirical mode decomposition (EEMD)* technique (Kolotkov et al. 2015).

Occulted coronal hard X-ray sources during Masuda-type flares (above the limb) have been observed not only in hard X-rays (with RHESSI), but also in microwaves (with NoRH), which both could be modeled with a single electron population that produces free-free bremsstrahlung and gyro-synchrotron emission, suggesting that the above-the-loop-top source is the electron acceleration region (Krucker et al. 2010). Taking the starting frequency of type III bursts into account, the height of the acceleration region was inferred to be well above the soft X-ray loop-top, i.e., at $h \approx 40$–60 Mm (Reid et al. 2011).

Evidence for a termination shock in standard solar flare models was put forward with high-cadence radio spectroscopy, where it is shown that a disruption of the shock coincides with an abrupt reduction of the energetic electron population (Chen et al. 2015).

Numerical simulation tools have been developed for modeling and forward-fitting of microwave and X-ray images, which allows to import magnetic field extrapolation models, to populate loops with non-uniform plasma densities and temperatures, as well as nonthermal electron distributions, and to compute radio and X-ray spectra, based on gyro-synchrotron emission, using SDO, NoRH, and RHESSI data (Nita et al. 2015).

For the 2011 September 23–24 flare, a filament was observed with a periodic alternate rotation in the clockwise and counter-clockwise directions with a 3-min period, which moreover was highly correlated with a 3-min global p-mode oscillation in a nearby sunspot (Kumar et al. 2016). It was suggested that the periodic reconnection at a magnetic null point causes the repetitive particle acceleration, the QPP observed in hard X-rays, microwaves, and type III radio bursts (Kumar et al. 2016).

12.10   White-Light Flares

"White light" refers to continuum emission in excess of the photospheric background. White-light flares have an excess intensity (normalized to local Quiet Sun values) by factors in the range of $\approx$ 0.1–4.1, in a sample of 11 events observed with TRACE and RHESSI during 2002–2004 (Hudson et al. 2006). TRACE was able to detect white-light flares by using the full broad-band response of the CCD sensor, producing images that were not compromised by ground-based seeing, and TRACE had excellent pointing stability, as well as high spatial (pixel size of $0.5''$) and temporal resolution. There is a strong association of the TRACE white-light emission (including UV and optical wavelengths) with hard X-ray sources observed with RHESSI. Although white-light emission is observed in the largest flares, it is also observed down to the GOES C1.6 class level. It is believed that white-light continuum is produced in essentially all flares, but its detection is subject to photon statistics, contrast, and background solar fluctuations (see reviews by Hudson et al. 2006, and Hudson 2016).

An earlier catalog of white-light flares has been compiled by using data from the aspect camera of the *Soft X-ray Telescope (SXT)* onboard Yohkoh, made in the Fraunhofer g-band with a pixel size of $2.46''$ and a typical sample interval of $\approx$ 10 s (Matthews et al. 2003). The catalog comprises 28 flare events, observed during 1991–1992, down to the GOES C7.8-class level. A maximum average contrast factor of 0.3 relative to the pre-flare continuum brightness was detected at the flare location. Comparing flares with and without white-light continuum, is was noted that white-light flare emission is also strongly related to coronal overpressure, indicating a component with a thermal, rather than a non-thermal origin (Matthews et al. 2003). On the other hand, a recent statistical study of 43 M- and X-class flares observed in hard X-rays (RHESSI) and white-light (HMI/SDO) has been conducted by Kuhar et al. (2016), which confirms a high correlation between the white-light flux and > 30 keV hard X-rays, or with the > 50 keV electron flux, and corroborates the interpretation that white-light emission is produced by > 50 keV electrons (Kuhar et al. 2016).

A white-light flare occurring on 2007 August 24 was observed with the *Swedish Solar Telescope (SST)* on La Palma, which acquired $H\alpha$ continuum with a sampling of $0.068''$ per pixel at the telescope's diffraction limit, and Ca II continuum with a sampling of $0.034''$ per pixel, both with a cadence of 0.12 s. Because of this much

higher spatial resolution than previously used (with TRACE), the flare displayed smaller kernels with a diameter of 300 km, with a contrast ratio of a factor 3 above the quiescent flux, and a delay of ≈ 2 min between the continuum emission of the impulsive flare phase and the chromospheric emission. It was concluded that the observed white-light emission is caused by radiative back-warming, and that white-light emission is a common feature of all solar flares (Jess et al. 2008).

A detailed analysis of the 2001 August 25, 16:30 UT, white-light flare observed with TRACE and HXT/Yohkoh concluded that the enhanced white-light emission originates in the chromosphere and temperature minimum region via nonequilibrium hydrogen ionization induced by direct collisions with the electron beam and by backwarming of the lower atmosphere. The three flare kernels observed in hard X-rays move along a magnetic separatrix at 400 km s^{-1}, which is considered as evidence of particle acceleration models that energize the electrons via magnetic reconnection at magnetic separators (Metcalf et al. 2003). In the 2003 October 29 white-light flare observed with the *Dunn Solar Telescope (DST)* at NSO/Sacramento Peak in near-infrared continuum at 1.56 μm, it was concluded that an interpretation in terms of back-warming is more likely than high-energy electron precipitation (Xu et al. 2004). On the other side, from analysis of the same flare it was concluded that photospheric heating by high-energy protons is likely to explain seismic emission from acoustically active flares (Donea and Lindsey 2005). Modeling a set of 9 white-light flares observed with RHESSI and TRACE led to the conclusion that the power required by the white-light luminosity enhancement is comparable to the electron beam power required to produce hard X-ray emission only if the low-energy cutoff to the spectrum is less than 25 keV, and thus such low-energy electrons cannot penetrate deep into a collisional thick-target, which places the co-spatial white-light sources into the upper chromosphere (Fletcher et al. 2007). The centroid heights of hard X-ray and white-light footpoints were directly measured (at the limb) to amount to $h = 305 \pm 170$ km (for ≈ 40 keV photons) and $h = 195 \pm 70$ km (at the opacity level of $\tau = 1$ of the 5000 Å wavelength) for the 2011 February 24, 07:35 UT, M3.5 flare (Martinez Oliveros et al. 2012), which is consistent with the electron beam precipitation model of white-light emission (Fig. 12.12). Another study finds altitudes of $h \approx 800$ km above the photosphere for co-spatial white-light and > 30 keV hard X-ray sources (Krucker et al. 2015).

Possible mechanisms of white-light emission are heating in the chromosphere causing optically thin or thick emission from free-bound transitions of hydrogen, and heating of the photosphere causing enhanced H^- continuum brightness. These processes were studied by combining observations from IRIS, HMI/SDO, Hinode, IBIS, and RHESSI, yielding blackbody temperatures of $T \approx 6000$–6300 K. The energy in > 40 keV electrons was found to be sufficient to explain the extra continuum emission of $(4$–$8) \times 10^{10}$ erg s^{-1} cm^{-2} (Kleint et al. 2016). For the X1.6-class flare of 2014 October 22, 14:02 UT, the deposited energy in nonthermal electrons was calculated to be $(3$–$7.7) \times 10^{10}$ erg cm^{-2} s^{-1} for a low-energy cutoff of 30–40 keV, while the energy flux estimated from the changes in temperature in the chromosphere (inferred from Mg II lines) was found to be 6%–22% of the deposited energy, which further confirms that the continuum enhancement is caused by $\gtrsim 30$
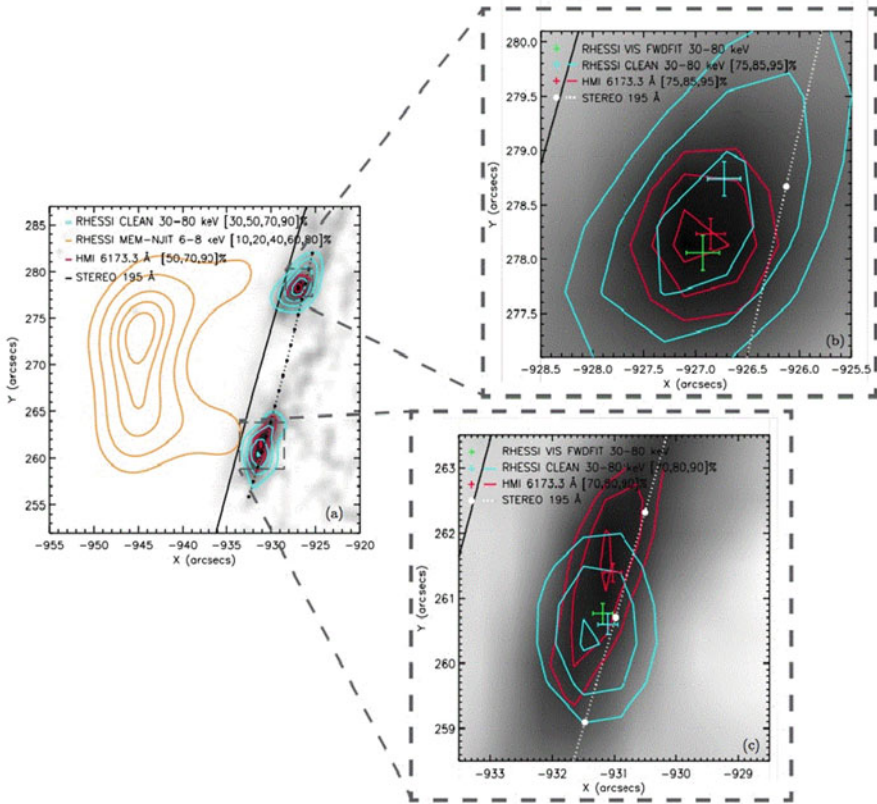
Fig. 12.12 HMI intensity continuum difference images (grey scale), white-light difference images (red), and RHESSI hard X-ray images 30–80 keV (blue), soft X-ray 6–8 keV RHESSI image (orange), and EUVI/STEREO source positions (white dots), of the 2011 February 24, 07:35 UT, flare (Martinez Oliveros et al. 2012)

keV nonthermal electrons (Lee et al. 2017). Recent numerical simulations with *radiative hydrodynamic (RHD)* codes investigate various emission mechanisms for white-light flares, such as hydrogen recombination continuum (Paschen) or the Thomson continuum due to scattering of disk radiation on flare electrons. For electron densities higher than 10^{12} cm^{-3}, the Paschen recombination continuum significantly dominates the Thomson scattering continuum (Heinzel et al. 2017).

Sampling the solar irradiance fluctuations in white-light with SOHO and GOES during solar flares, using a superposed epoch analysis, the white-light emission was found to be consistent with blackbody emission at $T \approx 9000$ K, while the white-light emission amounts to about 70% of the total radiated energy (Kretzschmar 2011). Using SOT/Hinode with optical continuum data taken in broadband red, green, and blue filters, blackbody temperatures of $T \approx 5000$–6000 K and a power of $E \approx 10^{26}$ erg emitted in optical wavelengths were found (Kerr and Fletcher 2014).

Statistical correlations between flare energies E and durations τ were determined in white-light superflares on solar-type stars also, and was found to be similar for both the Sun and the stars, i.e., $\tau \propto E^{0.4}$.

Velocity and magnetic transients were detected near the umbral boundary of the main sunspot during white-light flares with HMI/SDO, which are related to line profile changes of the Stokes parameters (Maurya et al. 2012).

Besides white-light (chromospheric) footpoint sources, there exist also (rarely reported) white-light ejecta, which are seen in coronal heights as continuum emission, rather than as line emission (Martinez Oliveros et al. 2014).

References

(12.1) Flare Gamma-Rays

Ackermann, M., Ajello, M., Albert, A., et al. 2014, *High-energy gamma-ray emission from solar flares: Summary of Fermi Large Area Telescope (LAT) detections and analysis of two M-class flares*, ApJ 787, 15, [46 c, 13 c/y].

Ackermann, M., Allafort, A., Baldini, L., et al. 2017, *Fermi-LAT observations of high-energy behind-the-limb solar flares*, ApJ 835, 219, [13 c, 13 c/y].

Ajello, M., Albert, A., Allafort, A., et al. 2014, *Impulsive and long duration high-energy emission from the very bright 2012 March 7 solar flares*, ApJ 789, 20, [53 c, 15 c/y].

Holman, G.D., Aschwanden, M.J., Aurass, H., et al. 2011, *Implications of X-ray observations for electron acceleration and propagation in solar flares*, SSRv 159, 107, [146 c, 22 c/y].

Holman, G.D. 2016, *Scientific considerations for future spectroscopic measurements from space of activity on the Sun*, JGR 121/12, 11,667, [7 c, 5 c/y].

Hurford, G.J., Schwartz, R.A., Krucker, S., et al. 2003, *First gamma-ray images of a solar flare*, ApJ 595, L77, [96 c, 7 c/y].

Hurford, G.J., Krucker, S., Lin, R.P., et al. 2006, *Gamma-ray imaging of the 2003 October/November solar flares*, ApJ 644, L93, [84 c, 7 c/y].

Kurt, V.G., Yushkov, B.Y., Kudela, K., et al. 2010, *High-energy gamma radiation of solar flares as an indicator of acceleration of energetic protons*, Cosmic Research 48, 70, [15 c, 2 c/y].

Kuznetsov, A.A., Nita, G.M., and Fleishman, G.D. 2011, *Gamma-ray and high-energy neutron measurements on CORONAS-F during the solar flare of 28 October 2003*, SoPh 268, 175, [24 c, 4 c/y].

Lin, R.P., Krucker, S., Hurford, G.J., et al. 2003, *RHESSI observations of particle acceleration and energy release in an intense solar gamma-ray line flare*, ApJ 595, L69, [264 c, 18 c/y].

Lin, R.P. 2006, *Particle acceleration by the Sun: Electrons, hard X-ray / Gamma-rays*, SSRv 124, 233, [19 c, 2 c/y].

Masson, S., Klein, K.L., Bütikofer, R., et al. 2009, *Acceleration of relativistic protons during the 20 January 2005 flare and CME*, SoPh 257, 305, [30 c, 4 c/y].

Murphy, R.J., Kozlovsky, B., Share, G.H., et al. 2007, *Using gamma-ray and neutron emission to determine solar flare accelerated particle spectra and composition and the conditions within the flare magnetic loop*, ApJSS 168, 167, [41 c, 4 c/y].

Nakariakov, V.M., Foullon, C., Myagkova, I.N., et al. 2010, *Quasi-periodic pulsations in the gamma-ray emission of a solar flare*, ApJ 708, L47, [44 c, 6 c/y].

Pesce-Rollins, M., Omodei, N., Petrosian, V., et al. 2015, *First detection of $\geq$ 100 MeV gamma rays associated with a behind-the-limb solar flare*, ApJ 805, L15, [20 c, 8 c/y].

Schrijver, C.J., Hudson, H.S., Murphy, R.J., et al. 2006, *Gamma rays and the evolving, compact structure of the 2003 October 28 X17 flare*, ApJ 650, 1184, [20 c, 2 c/y].

Share, G.H., Murphy, R.J., Smith, D.M., et al. 2004, *RHESSI e+e- annihilation radiation observations: Implications for conditions in the flaring solar chromosphere*, ApJ 615, L169, [40 c, 3 c/y].

Shih, A.Y., Lin, R.P., and Smith, D.M. 2009, *RHESSI observations of the proportional acceleration of relativistic > 0.3 MeV electrons and > 30 MeV protons in solar flares*, ApJ 698, L152, [51 c, 6 c/y].

Smith, D.M., Share, G.H., Murphy, R.J., et al. 2003, *High-resolution spectroscopy of gamma-ray lines from the X-class solar flare of 2002 July 23*, ApJ 595, L81, [61 c, 4 c/y].

Tatischeff, V., Kozlovsky, B., Kiener, J., et al. 2006, *Delayed X- and gamma-ray line emission from solar flare radioactivity*, ApJSS 165, 606, [24 c, 2 c/y].

Trottet, G., Krucker, S., Lüthi, T., et al. 2008, *Radio submillimeter and gamma-ray observations of the 2003 October 28 solar flare*, ApJ 678, 509, [35 c, 4 c/y].

Vilmer, N., MacKinnon, A.L., and Hurford, G.J. 2011, *Properties of energetic ions in the solar atmosphere from gamma-ray and neutron observations*, SSRv 159, 167, [56 c, 9 c/y].

(12.2) Flare Hard X-Ray Ribbons

Asai, A., Isii, T.T., Kurokawa, H., et al. 2003, *Evolution of conjugate footpoints inside flare ribbons during a great two-ribbon flare on 2001 April 10*, ApJ 586, 624, [44 c, 3 c/y].

Asai, A., Yokoyama, T., Shimojo, M., et al. 2004, *Flare ribbon expansion and energy release rate*, ApJ 611, 557, [71 c, 5 c/y].

Aschwanden, M.J. and Alexander, D. 2001, *Flare plasma cooling from 30 MK down to 1 MK modeled from Yohkoh, GOES, and TRACE observations during the Bastille Day event (14 July 2000)*, SoPh 204, 91, [122 c, 7 c/y].

Dennis, B.R. and Pernak, R.L. 2009, *Hard X-ray flare source sizes measured with the RHESSI*, ApJ 698, 2131, [61 c, 7 c/y].

Fletcher, L. and Hudson, H.S. 2001, *The magnetic structure and generation of EUV flare ribbons*, SoPh 204, 69, [104 c, 6 c/y].

Fletcher, L. and Hudson, H.S. 2002, *Spectral and spatial variations of flare hard X-ray footpoints*, SoPh 210, 307, [84 c, 5 c/y].

Fletcher, L., Dennis, B.R., Hudson, H.S., et al. 2011, *An observational overview of solar flares*, SSRv 159, 19, [238 c, 37 c/y].

Fletcher, L., Hannah, I.G., Hudson, H.S., et al. 2013, *Flare ribbon energetics in the early phase of an SDO flare*, ApJ 771, 104, [22 c, 5 c/y].

Gallagher, P.T., Dennis, B.R., Krucker, S. et al. 2002, *RHESSI and TRACE observations of the 21 April 2002 X1.5 flare*, SoPh 210, 341, [97 c, 6 c/y].

Grigis, P.C. and Benz, A.O. 2005, *The evolution of reconnection along an arcade of magnetic loops*, ApJ 625, L143, [82 c, 7 c/y].

Jing, J., Lee, J., Liu, C., et al. 2007, *Hard X-ray intensity distribution along Hα ribbons*, ApJ 664, L127, [21 c, 2 c/y].

Kontar, E.P., MacKinnon, A.L., Schwartz, R.A., et al. 2006, *Compton backscattered and primary X-rays from solar flares: angle dependent Green's function correction for photospheric albedo*, A&A 446, 1157, [68 c, 6 c/y].

Krucker, S., Hurford, G.J., and Lin, R.P. 2003, *Hard X-ray source motions in the 2002 July 23 Gamma-ray flare*, ApJ 595, L103, [119 c, 8 c/y].

Krucker, S., Hudson, H.S., Jeffrey, N.L.S. 2011, *High-resolution imaging of solar flare ribbons and its implications on the thick-target model*, ApJ 739, 96, [69 c, 11 c/y].

Liu, C., Lee, J., Gary, D., et al. 2007, *The ribbon-like hard X-ray emission in a sigmoidal solar active region*, ApJ 658, L127, [28 c, 3 c/y].

Liu, C., Lee, J., Jing, J. et al. 2008, *The spatial distribution of the hard X-ray spectral index and the local magnetic reconnection rate*, ApJ 672, L69, [12 c, 1 c/y].

Masuda, S., Kosugi, T., and Hudson, H.S. 2001, *A hard X-ray two-ribbon flare observed with Yohkoh/HXT*, SoPh 204, 55, [71 c, 4 c/y].

Qiu, J. and Cheng, J. 2017, *Gradual solar coronal dimming and evolution of coronal mass ejection in the early phase*, ApJ 838, L6, [2 c, 2 c/y].

Savcheva, A., Pariat, E., McKillop, S., et al. 2015, *The relation between solar eruption topologies and observed flare features. I. Flare ribbons*, ApJ 810, 96, [36 c, 14 c/y].

Savcheva, A., Pariat, E., McKillop, S., et al. 2016, *The relation between solar eruption topologies and observed flare features. II. Dynamical evolution*, ApJ 817, 43, [20 c, 13 c/y].

Temmer, M., Veronig, A.M., Vrsnak, B., et al. 2007, *Energy release rates along Hα ribbons and the location of hard X-ray sources*, ApJ 654, 665, [43 c, 5 c/y].

Wang, H. and Liu, C. 2012, *Circular ribbon flares and homologous jets*, ApJ 760, 101, [65 c, 12 c/y].

Warren, H.P. and Warshall, A.D. 2001, *Ultraviolet flare ribbon brightenings and the onset of hard X-ray emission*, ApJ 560, 87, [43 c, 3 c/y].

Yang, K., Guo, Y., and Ding, M.D. 2015, *On the 2012 October 23 circular ribbon flare: Emission features and magnetic topology*, ApJ 806, 171, [27 c, 11 c/y].

(12.3) Coronal Hard X-Rays

Asai, A., Yokoyama, T., Shimojo, M., et al. 2004, *Downflow motions associated with impulsive nonthermal emissions observed in the 2002 July 23 solar flare*, ApJ 605, L77, [119 c, 9 c/y].

Aschwanden, M.J., Hudson, H.S., Kosugi, T., et al. 1996, *Electron time-of-flight measurements during the Masuda flare, 1992 January 13*, ApJ 464, 985, [74 c, 3 c/y].

Bain, H.M. and Fletcher, L. 2009, *Hard X-ray emission from a flare-related jet*, A&A 508, 1443, [16 c, 2 c/y].

Battaglia, M. and Benz, A.O. 2006, *Relations between concurrent hard X-ray sources in solar flares*, A&A 456, 751, [83 c, 7 c/y].

Battaglia, M. and Benz, A.O. 2007, *Exploring the connection between coronal and footpoint sources in a thin-thick target solar flare model*, A&A 466, 713, [22 c, 2 c/y].

Caspi, A. and Lin, R.P. 2010, *RHESSI line and continuum observations of super-hot flare plasma*, ApJ 725, L161, [71 c, 9 c/y].

Ishikawa, S., Krucker, S., Takahashi, T., et al. 2011, *On the relation of above-the-loop and footpoint hard X-ray sources in solar flares*, ApJ 737, 48, [20 c, 3 c/y].

Ji, H., Wang, H., Liu, C., et al. 2008, *A hard X-ray sigmoidal structure during the initial phase of the 2003 October 29 X10 flare*, ApJ 680, 734, [30 c, 3 c/y].

Krucker, S., White, S.M., and Lin, R.P. 2007a, *Solar flare hard X-ray emission from the high corona*, ApJ 669, L49, [38 c, 4 c/y].

Krucker, S., Hannah, I.G., and Lin, R.P. 2007b, *RHESSI and Hinode X-ray observations of a partially occulted solar flare*, ApJ 671, L193, [18 c, 2 c/y].

Krucker, S. and Lin, R.L. 2008, *Hard X-ray emissions from partially occulted solar flares*, ApJ 673, 1181, [84 c, 9 c/y].

Krucker, S., Battaglia, M., Cargill, P.J., et al. 2008, *Hard X-ray emission from the solar corona*, A&AR 16, 155, [123 c, 13 c/y].

Krucker, S., Hudson, H.S., Glesener, L., et al. 2010, *Measurements of the coronal acceleration region of a solar flare*, ApJ 714, 1108, [109 c, 15 c/y].

Lin, R.P., Krucker, S., Hurford, G.J., et al. 2003, *RHESSI observations of particle acceleration and energy release in an intense solar gamma-ray line flare*, ApJ 595, L69, [264 c, 28 c/y].

Liu, W., Petrosian, V., Dennis, B.R., et al. 2008, *Double coronal hard and soft X-ray source observed by RHESSI: Evidence for magnetic reconnection and particle acceleration in solar flares*, ApJ 676, 704, [75 c, 8 c/y].

Masuda, S., Kosugi, T., Hara, H., et al. 1994, *A loop-top hard X-ray source in a compact solar flare as evidence for magnetic reconnection*, Nature 371, 495, [726 c, 31 c/y].

Sui, L., and Holman, G.D. 2003, *Evidence for the formation of a large-scale current sheet in a solar flare*, ApJ 596, 251, [223 c, 14 c/y].

Sui, L., Holman, G.D., Dennis, B.R. 2004, *Evidence for magnetic reconnection in three homologous solar flares observed by RHESSI*, ApJ 612, 546, [167 c, 12 c/y].

Veronig, A.M. and Brown, J.C. 2004, *A coronal thick-target interpretation of two hard X-ray loop events*, ApJ 603, L117, [127 c, 9 c/y].

Veronig, A.M., Karlicky, M., Vrsnak, B., et al. 2006, *X-ray sources and magnetic reconnection in the X3.9 flare of 2003 November 3*, A&A 446, 675, [97 c, 8 c/y].

(12.4) Modeling of Hard X-ray Spectra

Aschwanden, M.J., Bynum, R.M., Kosugi, T., et al. 1997, *Electron trapping times and trap densities in solar flare loops measured with Compton and Yohkoh*, ApJ 487, 936, [60 c, 3 c/y].

Aschwanden, M.J. 2007, *RHESSI timing studies: Multithermal delays*, ApJ 661, 1242, [24 c, 2 c/y].

Aschwanden, M.J., Holman, G., O'Flannagain, A., et al. 2016, *Global energetics of solar flares. III. Nonthermal energies*, ApJ 832, 27, [16 c, 11 c/y].

Bain, H.M. and Fletcher, L. 2009, *Hard X-ray emission from a flare-related jet*, A&A 508, 1443, [16 c, 2 c/y].

Chen, Q. and Petrosian, V. 2013, *Determination of stochastic acceleration model characteristics in solar flares*, ApJ 777, 33, [16 c, 4 c/y].

Dennis, B.R., Duval-Poo, M.A., Piana, M., et al. 2018, *Coronal hard X-ray sources revisited*, ApJ 867, 82.

Emslie, A.G. 2003, *The determination of the total injected power in solar flare electrons*, ApJ 595, L119, [41 c, 3 c/y].

Grigis, P.C. and Benz, A.O. 2004, *The spectral evolution of impulsive solar X-ray flares*, A&A 426, 1093, [98 c, 7 c/y].

Holman, G.D. 2003, *The effects of low- and high-energy cutoffs on solar flare microwave and hard X-ray spectra*, ApJ 586, 606, [71 c, 5 c/y].

Holman, G.D., Sui, L., Schwartz, R.A., et al. 2003, *Electron bremsstrahlung hard X-ray spectra, electron distributions, and energetics in the 2002 July 23 solar flare*, ApJ 595, L97, [213 c, 15 c/y].

Kasparova, J., Kontar, E.P., and Brown, J.C. 2007, *Hard X-ray spectra and positions of solar flares observed by RHESSI: photospheric albedo, directivity and electron spectra*, A&A 466, 705, [38 c, 4 c/y].

Kontar, E.P., Brown, J.C., and McArthur, G.K. 2002, *Nonuniform target ionization and fitting thick target electron injection spectra to RHESSI data*, SoPh 210, 419, [40 c, 3 c/y].

Kontar, E.P., MacKinnon, A.L., Schwartz, R.A., et al. 2006, *Compton backscattered and primary X-rays from solar flares: angle dependent Green's function correction for photospheric albedo*, A&A 446, 1157, [68 c, 6 c/y].

Kontar, E.P., Brown, J.C., Emslie, A.G., et al. 2011, *Deducing electron properties from hard X-ray observations*, SSRv 159, 301, [85 c, 13 c/y].

Kontar, E.P., Jeffrey, N.L.S., Emslie, A.G., et al. 2015, *Collisional relaxation of electrons in a warm plasma and accelerated nonthermal electron spectra in solar flares*, ApJ 809, 35, [12 c, 5 c/y].

Krucker, S. and Lin, R.L. 2008, *Hard X-ray emissions from partially occulted solar flares*, ApJ 673, 1181, [84 c, 9 c/y].

Massone, A.M., Emslie, A.G., Kontar, E.P., et al. 2004, *Anisotropic bremsstrahlung emission and the form of regularized electron flux spectra in solar flares*, ApJ 613, 1233, [31 c, 2 c/y].

Oka, M., Ishikawa, S., Saint-Hilaire, P., et al. 2013, *Kappa distribution model for hard X-ray coronal sources of solar flares*, ApJ 764, 6, [41 c, 9 c/y].

Petrosian, V. and Chen, Q. 2010, *Derivation of stochastic acceleration model characteristics for solar flares from RHESSI hard X-ray observations*, ApJ 712, L131, [20 c, 3 c/y].

Saint-Hilaire, P. and Benz, A.O. 2005, *Thermal and non-thermal energies of solar flares*, A&A 435, 743, [81 c, 6 c/y].

Su Y., Holman, G.D., and Dennis, B.R. 2011, *Evidence for the full hard X-ray spectral signature of nonuniform ionization in a solar flare*, Ap[J 731m 106, [13 c, 2 c/y].

Sui, L., Holman, G.D., and Dennis, B.R., et al. 2005, *Determination of low-energy cutoffs and total energy of nonthermal electrons in a solar flare on 2002 April 15*, ApJ 626, 1102, [57 c, 5 c/y].

Xu, Y., Emslie, A.G., and Hurford, G.J. 2008, *RHESSI hard X-ray imaging spectroscopy of extended sources and the physical properties of electron acceleration regions in solar flares*, ApJ 673, 576, [57 c, 6 c/y].

(12.5) Rapid Magnetic Changes During Flares

Aschwanden, M.J., Xu, Y., and Jing, J. 2014, *Global energetics of solar flares. I. Magnetic energies*, ApJ 797, 50, [27 c, 8 c/y].

Kleint, L. 2017, *First detection of chromospheric magnetic field changes during an X1-flare*, ApJ 834, 26, [7 c, 7 c/y].

Liu, C., Deng, N., Liu, Y., et al. 2005, *Rapid change of δ spot structure associated with 7 major flares*, ApJ 622, 722, [97 c, 8 c/y].

Liu, C., Deng, N., Liu, R., et al. 2012, *Rapid changes of photospheric magnetic field after tether-cutting reconnection and magnetic implosion*, ApJ 745, L4, [61 c, 11 c/y].

Petrie, G.J.D. 2013, *A spatio-temporal description of the abrupt changes in the photospheric magnetic and Lorentz-force vectors during the 15 February 2011 X2.2 flare*, SoPh 287, 415, [46 c, 8 c/y].

Petrie, G.J.D. 2014, *Estimating flare-related photospheric Lorentz force vector changes within active regions*, SoPh 289, 3663, [6 c, 2 c/y].

Schrijver, C.J., DeRosa, M.L., Metcalf, T., et al. 2008, *Nonlinear force-free field modeling of a solar active region around the time of a major flare and coronal mass ejection*, ApJ 675, 1637, [191 c, 20 c/y].

Sudol, J.J. and Harvey, J.W. 2005, *Longitudinal magnetic field changes accompanying solar flares*, ApJ 635, 647, [166 c, 13 c/y].

Sun, X., Hoeksema, J.T., Liu, Y., et al. 2012, *Evolution of magnetic field and energy in a major eruptive active region based on SDO/HMI observations*, ApJ 748, 77, [191 c, 34 c/y].

Sun, X., Bobra, M.G., Hoeksema, J.T., et al. 2015, *Why is the great solar active region 12192 flare-rich but CME-poor ?* ApJ 804, L28, [71 c, 28 c/y].

Wang, H., Spirock, T.J., Qiu, J., et al. 2002, *Rapid changes of magnetic fields associated with 6 X-class flares*, ApJ 576, 497, [104 c, 7 c/y].

Wang, H. 2006, *Rapid changes of photospheric magnetic fields around flaring magnetic neutral lines*, ApJ 649, 490, [78 c, 7 c/y].

Wang, H. and Liu, C. 2010, *Observational evidence of back reaction on the solar surface associated with coronal magnetic restructuring in solar eruptions*, ApJ 716, L195, [84 c, 11 c/y].

Wang, H., Liu, C., Ahn, K., et al. 2017, *High-resolution observations of flare precursors in the low solar atmosphere*, Nature Astronomy 1, 0085, [15 c, 15 c/y].

Wang, S., Liu, C., Lu, R., et al. 2012, *Response of the photospheric field to the X2.2 flare on 2002 February 15*, ApJ 745, L17, [95 c, 17 c/y].

Xu, Z, Yang, K., Guo, Y., et al. 2017, *Homogolous circular-ribbon flares driven by flux emergence*, ApJ 851, 30, [5 c, 5 c/y].

Yurchyshyn, V., Wang, H., Abramenko, V., et al. 2004, *Magnetic field, Hα, and RHESSI observations of the 2002 July 23 gamma-ray flare*, ApJ 605, 546, [42 c, 3 c/y].

(12.6) Magnetic Reconnection and Particle Acceleration

Aschwanden, M.J., Kosugi, T., Hudson, H.S., et al. 1996, *The scaling law between electron time-of-flight distances and loop lengths in solar flares*, ApJ 470, 1998, [78 c, 4 c/y].

Aulanier, G., Pariat, E., Démoulin, P., et al. 2006, *Slip-running reconnection in quasi-separatrix layers*, SoPh 238, 347, [136 c, 12 c/y].

Aulanier, G., Janvier, M., and Schmieder, B. 2012, *The standard flare model in 3-D. I. Strong-to-weak shear transition in post-flare loops*, A&A 543, A110, [80 c, 15 c/y].

Che, H., Drake, J.F., and Swisdak, M. 2011, *A current filamentation mechanism for breaking magnetic field lines during reconnection*, Nature 474, 184, [75 c, 12 c/y].

Chen, L.J., Bhattacharjee, A., Puhl-Quinn, P.A., et al. 2008, *Observation of energetic electrons within magnetic islands*, Nature Physics 4, 19, [130 c, 14 c/y].

Drake, J.F., Swisdak, M., Che, H., et al. 2006, *Electron acceleration from contracting magnetic islands during reconnection*, Nature 443, 553, [438 c, 38 c/y].

Drake, J.F., Swisdak, M., and Fermo, R. 2013, *The power-law spectra of energetic particles during multi-island magnetic reconnection*, ApJ 763, L5, [61 c, 14 c/y].

Dudik, J., Janvier, M., Aulanier, G., et al. 2014, *Slipping magnetic reconnection during an X-class flare observed by SDO/AIA*, ApJ 784, 144, [57 c, 16 c/y].

Fletcher, L. and Hudson, H.S. 2008, *Impulsive phase flare energy transport by large-scale Alfvén waves and the electron acceleration problem*, ApJ 675, 1645, [202 c, 21 c/y].

Janvier, M., Aulanier, G., Pariat, E., et al. 2013, *The standard flare model in 3-D: III. Slip-running reconnection properties*, A&A 555, A77, [66 c, 15 c/y].

Janvier, M., Aulanier, G., Bommer, V., et al. 2014, *Electric currents in flare ribbons: Observations and 3-D standard model*, ApJ 788, 60, [58 c, 16 c/y].

Janvier, M., Savcheva, A., Pariat, E., et al. 2016, *Evolution of flare ribbons, electric currents, and quasi-separatrix layers during an X-class flare*, A&A 591, A141, [15 c, 10 c/y].

Ji, H., Wang, H., Liu, C., et al. 2008, *A hard X-ray sigmoidal structure during the initial phase of the 2003 October 29 X10 flare*, ApJ 680, 734, [30 c, 3 c/y].

Kliem, B., Karlicky, M., and Benz, A.O. 2000, *Solar radio pulsations as a signature of dynamic magnetic reconnection*, A&A 360, 715, [280 c, 16 c/y].

Li, T. and Zhang, J. 2015, *Quasi-periodic slipping magnetic reconnection during an X-class solar flare observed by the SDO and IRIS*, ApJ 804, L8, [43 c, 17 c/y].

Li, Y., Qiu,J., Longcope, D.W., et al. 2016, *Observation of an X-shaped ribbon flare in the Sun and its 3-D magnetic reconnection*, ApJ 823, L13, [7 c, 5 c/y].

Liu, W., Petrosian, V., Dennis, B.R. 2008, *Double coronal hard and soft X-ray source observed by RHESSI: Evidence for magnetic reconnection and particle acceleration in solar flares*, ApJ 676, 704, [75 c, 8 c/y].

Qiu, J., Lee, J., Gary, E.D., et al. 2002, *Motion of flare footpoint emission and inferred electric field in reconnecting current sheets*, ApJ 656, 1335, [129 c, 8 c/y].

Shibata, K. and Tanuma, S. 2001, *Plasmoid-induced reconnection and fractal reconnection*, Earth, Planets and Space 53, 473, [247 c, 15 c/y].

Sui, L. and Holman, G.D. 2003, *Evidence for the formation of a large-scale current sheet in a solar flare*, ApJ 596, L251, [223 c, 15 c/y].

Sui, L., Holman, G.D., and Dennis, B.R. 2004, *Evidence for magnetic reconnection in three homologous solar flares observed by RHESSI*, ApJ 612, 546, [167 c, 12 c/t].

Sun, X., Hoeksema, J.T., Liu, Y., et al. 2013, *Hot spine loops and the nature of a late-phase solar flare*, ApJ 778, 139, [64 c, 14 c/y].

Takasao, S., Asai, A., Isobe, H., et al. 2012, *Simultaneous observation of reconnection inflow and outflow associated with the 2010 August 18 solar flare*, ApJ 745, L6, [73 c, 13 c/y].

Toriumi, S. and Takasao, S. 2017, *Numerical simulations of flare-productive regions: δ-sunspots, sheared polarity inversion lines, energy storage, and prediction*, ApJ 850, 39, [4 c, 4 c/y].

Toriumi, S., Schrijver, C.J., Harra, L.K. 2017, *Magnetic properties of solar active regions that govern large solar flares and eruptions*, ApJ 834, 56, [16 c, 16 c/y].

Veronig, A.M., Karlicky, M., Vrsnak, B., et al. 2006, *X-ray sources and magnetic reconnection in the X3.9 flare of 2003 November 3*, A&A 446, 675, [97 c, 8 c/y].

Yokoyama, T., Akita, K., Morimoto, T., et al. 2001, *Clear evidence of reconnection inflow of a solar flare*, ApJ 546, L69, [212 c, 13 c/y].

Zhao, J., Gilchrist, S.A., Aulanier, G., et al. 2016, *Hooked flare ribbons and flux-rope-related QSL footprints*, ApJ 823, 62, [19 c, 13 c/y].

(12.7) Microflares and Nanoflares

Aschwanden, M.J., Nightingale, R., Tarbell, T., et al. 2000a, *Time variability of the quiet Sun observed with TRACE. I. Instrumental effects, event detection, and discrimination of EUV nanoflares*, ApJ 535, 1027, [58 c, 3 c/y].

Aschwanden, M.J., Tarbell, T., Nightingale, R., et al. 2000b, *Time variability of the quiet Sun observed with TRACE. II. Physical parameters, temperature evolution, and energetics of EUV nanoflares*, ApJ 535, 1047, [219 c, 13 c/y].

Aschwanden, M.J. and Parnell, C.E. 2002, *Nanoflare statistics from first principles: Fractal geometry and temperature synthesis*, ApJ 572, 1048, [113 c, 7 c/y].

Battaglia, M., Grigis, P.C., and Benz, A.O. 2005, *Size dependence of solar X-ray flare properties*, A&A 439, 737, [67 c, 5 c/y].

Benz, A.O. and Grigis, P. 2002, *Microflares and hot component in solar active regions*, SoPh 210, 431, [41 c, 3 c/y].

Benz, A.O. and Krucker, S. 2002, *Energy distribution of microevents in the quiet solar corona*, ApJ 568, 413, [80 c, 5 c/y].

Christe, S., Hannah, I.G., Krucker, S., et al. 2008, *RHESSI microflares statistics. I. Flare-finding and frequency distributions*, ApJ 677, 1385, [71 c, 7 c/y].

Hannah, I.G., Hurford, G.J., Hudson, H.S., et al. 2007, *First limits on the 3–200 keV X-ray spectrum of the Quiet Sun using RHESSI*, ApJ 659, L77, [17 c, 2 c/y].

Hannah, I.G., Christe, S., Krucker, S., et al. 2008, *RHESSI microflare statistics. II. X-ray imaging, spectroscopy, and energy distribution*, ApJ 677, 704, [98 c, 10 c/y].

Hannah, I.G., Hudson, H.S., Hurford, G.J., et al. 2010, *Constraining the hard X-ray properties of the Quiet Sun with new RHESSI observations*, ApJ 724, 487, [25 c, 3 c/y].

Hannah, I.G., Hudson, H.S., Battaglia, M., et al. 2011, *Microflares and the statistics of X-ray flares*, SSRv 159, 263, [60 c, 9 c/y].

Hudson, H.S. 1991, *Solar flares, microflares, nanoflares, and coronal heating*, SoPh 133, 357, [358 c, 14 c/y].

Jing, J., Xu, Y., Cao, W., et al. 2016, *Unprecedented fine structure of a solar flare revealed by the 1.6 m New Solar Telescope*, Scientific Reports 6, 24319, [25 c, 17 c/y].

Krucker, S. and Benz, A.O. 1998, *Energy distribution of heating processes in the quiet solar corona*, ApJ 501, L213, [195 c, 10 c/y].

Krucker, S. and Benz, A.O. 2000, *Are heating events in the quiet solar corona small flares? Multiwavelength observations of individual events*, SoPh 191, 341, [55 c, 3 c/y].

Krucker, S., Christe, S., Lin, R.P. 2002, *Hard X-ray microflares down to 3 keV*, SoPh 210, 445, [54 c, 3 c/y].

McTiernan, J.M. 2009, *RHESSI/GOES observations of the nonflaring Sun from 2002 to 2006*, ApJ 697, 94, [41 c, 5 c/y].

Parnell, C.E. and Jupp, P.E. 2000, *Statistical analysis of the energy distribution of nanoflares in the Quiet Sun*, ApJ 529, 554, [193 c, 11 c/y].

Polito, V., Reeves, K.K., Del Zanna, G., et al. 2015, *Joint high temperature observation of a small C6.5 solar flare with IRIS/EIS/AIA*, ApJ 803, 84, [26 c, 10 c/y].

Reale, F., McTiernan, J.M., and Testa, P. 2009, *Comparison of Hinode/XRT and RHESSI detection of hot plasma in the non-flaring solar corona*, ApJ 704, L58, [29 c, 3 c/y].

Ryan,D.F., O'Flannagain,A.M., Aschwanden, M.J., Gallagher,P.T. 2014, *The compatibility of flare temperatures observed with AIA, GOES, and RHESSI*, SoPh 289, 2547, [15 c, 4 c/y].

Stoiser, S., Veronig, A.M., Aurass, H., et al. 2007. *RHESSI microflares: I. X-ray properties and multiwavelength characteristics*, SoPh 246, 339, [10 c, 1 c/y].

Testa, P., De Pontieu, B., Allred, J., et al. 2014, *Evidence of nonthermal particles in coronal loops heated impulsively by nanoflares*, Science 346, 1255724, [50 c, 14 c/y].

Young, P.R., Tian, H., and Jaeggli, S. 2015, *The 2014 March 29 X-flare: Subarcsecond resolution observations of Fe XXI λ1354.1*, ApJ 799, 218, [42 c, 17 c/y].

(12.8) Flare Hard X-Ray Oscillations

Asai, A., Shimojo, M., Isobe, H., et al. 2001, *Periodic acceleration of electrons in the 1998 November 10 solar flare*, ApJ 562, L103, [91 c, 6 c/y].

Aschwanden, M.J. 1987, *Theory of radio pulsations in coronal loops* SoPh 111, 113, [214 c, 7 c/y].

Brosius, J.W., Daw, A.N., and Inglis, A.R. 2016, *Quasi-periodic fluctuations and chromospheric evaporation in a solar flare ribbon observed by Hinode/EIS, IRIS, and RHESSI*, ApJ 830, 101, [14 c, 9 c/y].

Dauphin, C., Vilmer, N., Lüthi, T., et al. 2005, *Modulations of broad-band radio continua and X-ray emissions in the large X-ray flare on 03 November 2003*, Adv.Spac.Res. 35, 1805, [10 c, 1 c/y].

Dennis, B.R., Tolbert, A.K., Inglis, A., et al. 2017, *Detection and interpretation of long-lived X-ray quasi-periodic pulsations in the X-class solar flare on 2013 May 14*, ApJ 836, 84, [9 c, 9 c/y].

Dolla, L., Marque, C., Seaton, D.B., et al. 2012, *Time delays in quasi-periodic pulsations observed during the X2.2 solar flare on 2011 February 15*. ApJ 749, L16, [30 c, 5 c/y].

Farnik, F., Karlicky, M., and Svestka, Z. 2003, *Hard X-ray pulsations in the initial phase of flares*, SoPh 218, 183, [18 c, 1 c/y].

Fleishman, G.D., Bastian, T.S., and Gary, D.E. 2008, *Broadband quasi-periodic radio and X-ray pulsations in a solar flare*, ApJ 684, 1433, [32 c, 3 c/y].

Foullon, C., Verwichte, E., Nakariakov, V.M. et al., 2005, *X-ray quasi-periodic pulsations in solar flares as MHD oscillations*, A&A 440, L59, [54 c, 4 c/y].

Foullon, C., Fletcher, L., Hannah, I.G., et al. 2010, *From large-scale loops to the sites of dense flaring loops: Preferential conditions for long-period pulsations in solar flares*, ApJ 719, 151, [18 c, 2 c/y].

Hayes, L.A., Gallagher, P.T., Dennis, B.R. et al. 2016, *Quasi-periodic pulsations during the impulsive and decay phases of an X-class flare*, ApJ 827, L30, [16 c, 11 c/y].

Gruber, D., Lachowica, P., Bissaldi, et al. 2011, *Quasi-periodic pulsations in solar flares: New clues from the Fermi Gamma-Ray Burst Monitor*, A&A 533. A61, [27 c, 4 c/y].

Inglis, A.R., Nakariakov, V.M., and Melnikov, V.F. 2008, *Multi-wavelength spatially resolved analysis of quasi-periodic pulsations in a solar flare*, A&A 487, 1147, [50 c, 5 c/y].

Inglis, A.R. and Gilbert, H.R. 2013, *Hard X-ray and ultraviolet emission during the 2011 June 6 solar flare*, ApJ 777, 30, [17 c, 4 c/y].

Inglis, A.R. and Dennis, B.R. 2012, *The relationship between hard X-ray pulse timings and the locations of footpoint sources during flares*, ApJ 748, 139, [11 c, 2 c/y].

Kumar, P., Nakariakov, V.M., and Cho, K.S. 2016, *Observation of a quasi-periodic pulsation in hard X-ray, radio, and EUV'*, ApJ 822, 7, [16 c, 11 c/y].

Kuznetsov, S.A., Zimovets, I.V., Morgachev, A.S., et al. 2016, *Spatio-temporal dynamics of sources of hard X-ray pulsations in solar flares*, SoPh 291, 3385, [6 c, 4 c/y].

Jakimiec,J. and Tomczak, M. 2010, *Investigation of quasi-periodic variations in hard X-rays of solar flares*, SoPh 261, 233, [13 c, 2 c/y].

Jakimiec,J. and Tomczak, M. 2012, *Investigation of quasi-periodic variations in hard X-rays of solar flares II. Further investigation of oscillating magnetic traps*, SoPh 278, 393, [5 c, 1 c/y].

Li, D., Ning, Z.J., and Zhang, Q.M. 2015, *Imaging and spectral observations of quasi-periodic pulsations in a solar flare*, ApJ 807, 72, [23 c, 9 c/y].

Li, Y.P. and Gan, W.Q. 2008, *Observational studies of the X-ray quasi-periodic oscillations of a solar flare*, SoPh 247, 77, [20 c, 3 c/y].

Nakariakov, V.M., Foullon, C., Myagkova, I.N., et al. 2010, *Quasi-periodic pulsations in the gamma-ray emission of a solar flare*, ApJ 708, L47, [45 c, 6 c/y].

Nakariakov, V.M. and Melnikov, V.F. 2009, *Quasi-periodic pulsations in solar flares*, SSRv 149, 119, [187 c, 21 c/y].

Nakariakov, V.M. and Zimovets, I.V., 2011, *Slow magneto-acoustic waves in two-ribbon flares*, ApJ 730, L27, [41 c, 6 c/y].

Ning, Z. 2014, *Imaging observations of X-ray quasi-periodic oscillations at 3–6 keV in the 26 December 2000 solar flare*, SoPh 289, 1239, [15 c, 4 c/y].

Ofman, L. and Sui, L. 2006, *Oscillations of hard X-ray flare emission observed by RHESSI: Effects of super-Alfvénic beams ?* ApJ 644, L149, [45 c, 4 c/y].

Terekhov, O.V., Shevchenko, A.V., Kuzmin, A.G. et al. 2002, *Observation of quasi-periodic pulsations in the flare SF 900610*, Astron.Lett. 28, 397, [11 c, 0.7 c/y].

Zimovets, I.V. and Struminsky, A.B. 2010, *Observations of double-periodic X-ray emission in interacting systems of solar flare loops*, SoPh 263, 163, [16 c, 2 c/y].

(12.9) Flare Radio Emission

Asai, A., Kiyohara, J., Takasaki, H., et al. 2013, *Temporal and spatial analyses of spectral indices of nonthermal emissions derived from hard X-rays and microwaves*, ApJ 763, 87, [17 c, 4 c/y].

Bastian, T.S., Fleishman, G.D., and Gary, D.E. 2007, *Radio spectral evolution of an X-ray poor impulsive solar flare: Implications for plasma heating and electron acceleration*, ApJ 666, 1256, [33 c, 3 c/y].

Benz, A.O., Grigis, P.C., Csillaghy, A., et al. 2005, *Survey on solar X-ray flares and associated coherent radio emissions*, SoPh 226, 121, [55 c, 4 c/y].

Chen, B., Bastian, T.S., Chen, C. 2015, *Particle acceleration by a solar flare termination shock*, Science 350, 1238, [20 c, 8 c/y].

Chernov, G.P. 2006, *Solar radio bursts with drifting stripes in emission and absorption*, SSRv 127, 195, [64 c, 6 c/y].

Fleishman, G.D., Bastian, T.S., and Gary, D.E. 2008, *Broadband quasi-periodic radio and X-ray pulsations in a solar flare*, ApJ 684, 1433, [32 c, 3 c/y].

Holman, G.D. 2003, *The effects of low- and high-energy cutoffs on solar flare microwave and hard X-ray spectra*, ApJ 586, 606, [71 c, 5 c/y].

Inglis, A.R., Nakariakov, V.M., and Melnikov, V.F. 2008, *Multi-wavelength spatially resolved analysis of quasi-periodic pulsations in a solar flare*, A&A 487, 1147, [50 c, 5 c/y].

Inglis, A.R., Ireland, J., Dominique, M. 2015, *Quasi-periodic pulsations in solar and stellar flares: Re-evaluating their nature in the context of power-law flare Fourier spectra*, ApJ 798, 108, [28 c, 11 c/y].

Karlicky, M. and Kliem, B. 2010. *Reconnection of a kinking flux rope triggering the ejection of a microwave and hard X-ray source. I. Observations and interpretation*, SoPh 266, 71, [30 c. 4 c/y].

Karlicky, M., Barta, M., and Rybak, J. 2010, *Radio spectra generated during coalescence processes of plasmoids in a flare current sheet*, A&A 514, 28, [23 c, 3 c/y].

Karlicky, M. and Barta, M. 2011, *Successive merging of plasmoids and fragmentation in a flare current sheet and their X-ray and radio signatures*, ApJ 733, 107, [32 c, 5 c/y].

Kliem, B., Karlicky, M., and Benz, A.O. 2000, *Solar radio pulsations as a signature of dynamic magnetic reconnection*, A&A 360, 715, [280 c, 16 c/y].

Kliem, B., Linton, M.G., Török, T., et al. 2010, *Reconnection of a kinking flux rope triggering the ejection of a microwave and hard X-ray source. II. Numerical modeling*, SoPh 266, 91, [41 cm, 5 c/y].

Kolotkov, D.Y., Nakariakov, V.M., Kupriyanova, E.G., et al. 2015, *Multi-mode quasi-periodic pulsations in a solar flare*, A&A 574, A53, [25 c, 10 c/y].

Krucker, S., Hudson, H.S., Glesener, L., et al. 2010, *Measurements of the coronal acceleration region of a solar flare*, ApJ 714, 1108, [109 c, 15 c/y].

Kumar, P., Nakariakov, V.M., Cho, K.S. 2016, *Observation of a quasiperiodic pulsation in hard X-ray, radio, and EUV wavelengths*, ApJ 822, 7, 16 c, 11 c/y].

Li, Y.P. and Gan, W.Q. 2005, *The shrinkage of flare radio loops*, ApJ 629, 137, [48 c, 4 c/y].

Nindos, A., Aurass, H., Klein, K.L. et al. 2008, *Radio emission of flares and coronal mass ejections. Invited review*, SoPh 253, 3, [48 c, 5 c/y].

Nita, G.M., Gary, D.E., and Lee, J.W. 2004, *Statistical study of two years of solar flare spectra obtained with the Owens Valley Solar Array (OVRA)*, ApJ 605, 528, [62 c, 5 c/y].

Nita, G.M., Fleishman, G.D., Kuznetsov, A.A. et al. 2015, *3-D radio and X-ray modelling and data analysis software: Revealing flare complexity*, ApJ 799, 236, [28 c, 11 c/y].

Reid, H.A.S., Vilmer, N., and Kontar, E.P. 2011, *Characteristics of the flare acceleration region derived from simultaneous hard X-ray and radio observations*, A&A 529, 66, [28 c, 4 c/y].

White, S.M., Benz, A.O., Christe, S., et al., 2011, *The relationship between solar radio and hard X-ray emission*, SSRv 159, 225, [62 c, 10 c/y].

Yu, S., Nakariakov, V.M., an Yan, Y. 2016, *Effect of a sausage oscillation on radio zebra pattern structures in a solar flare*, ApJ 826, 78, [6 c, 4 c/y].

(12.10) White-Light Flares

Donea, A.C. and Lindsey, C. 2005, *Seismic emission from the solar flares of 2003 October 28 and 29*, ApJ 630, 1168, [92 c, 7 c/y].

Fletcher, L., Hannah, I.G., Hudson, H.S., et al. 2007, *A TRACE white light and RHESSI hard X-ray study of flare energetics*, ApJ 656, 1187, [88 c, 8 c/y].

Heinzel, P., Kleint, L., Kasparova, J., et al. 2017, *On the nature of off-limb flare continuum sources detected by SDO/HMI*, ApJ 847, 48, [4 c, 4 c/y].

Hudson, H.S., Wolfson, C.J., and Metcalf, T.R. 2006, *White-light flares: A TRACE/ RHESSI overview*, SoPh 234, 79, [82 c, 7 c/y].

Hudson, H.S. 2016, *Chasing white-light flares*, SoPh 291, 1273, [8 c, 5 c/y].

Jess, D.B., Mathioudakis, M., Crockett, P.J., et al. 2008, *Do all flares have white-light emission ?* ApJ 688, 119, [62 c, 7 c/y].

Kerr, G.S. and Fletcher, L. 2014, *Physical properties of white-light sources in the 2011 February 15 solar flare*, ApJ 783, 98, [28 c, 8 c/y].

Kleint, L., Heinzel, P., Judge, P., et al. 2016, *Continuum enhancements in the ultraviolet, the visible and the infrared during the X1 flare on 2014 March 29*, ApJ 816, 88, [28 c, 19 c/y].

Kretzschmar, M. 2011, *The Sun as a star: Observations of white-light flares*, A&A 530, 84, [64 c, 10 c/y].

Krucker, S., Saint-Hilaire, P., Hudson, H.S., 2015, *Cospatial white light and hard X-ray flare footpoints seen above the solar limb*, ApJ 802, 19, [26 c, 10 c/y].

Kuhar, M., Krucker, S., Martinez Oliveros, J.C., et al. 2016, *Correlation of hard X-ray and white-light emission in solar flares*, ApJ 816, 6, [21 c, 14 c/y].

Lee, K.S., Imada, S., Watanabe, K., et al. 2017, *IRIS, Hinode, SDO, and RHESSI observations of a white light flare produced directly by nonthermal electrons*, ApJ 836, 150, [13 c, 13 c/y].

Martinez Oliveros, J.C., Hudson, H.S., Hurford, G.J., et al., 2012, *The height of a white-light flare and its hard X-ray sources*, ApJ 753, 26, [49 c, 9 c/y].

Martinez Oliveros, J.C., Krucker, S., Hudson, H.S., et al. 2014, *Chromospheric and coronal observations of solar flares with the HMI*, ApJ 780, L28, [12 c, 3 c/y].

Matthews, S.A., van Driel-Gesztelyi, L., Hudson, H.S., et al. 2003, *A catalogue of white-light flares observed by Yohkoh*, A&A 409, 1107, [51 c, 4 c/y].

Metcalf, T.R., Alexander, D., Hudson, H.S., et al. 2003, *TRACE and Yohkoh observations of a white-light flare*, ApJ 595, 483, [90 c, 6 c/y].

Maurya, R.A., Vemareddy, P., and Ambastha, A. 2012, *Velocity and magnetic transient driven by the X2.2 white-light flare of 2011 February 15 in NOAA 11158*, ApJ 747, 134, [36 c, 7 c/y].

Xu, Y., Cao, W., Liu,C., et al. 2004, *Near-infrared observations at 1.56 microns of the 2003 October 29 X10 white-light flare*, ApJ 607, L131, [69 c, 5 c/y].